VOLCANICA Article in Press

This is an uncorrected proof, meaning that this manuscript has not been copyedited or formatted according to Volcanica's styles and standards. In turn, this means that article content, including text, may still change prior to final publication. Although articles in press do not have all bibliographic details available yet, they can be cited using the year of online publication and the DOI, as follows: author(s), (year), article title, Volcanica, DOI.

Vlastelic, I., Piro, J.-L., Famin, V., Berthod, C., Bachèlery, P., Rouyer, T. and Di Muro, A. (2026) “Chalcogen element (S – Se – Te) constraints on the source of the Fani Maoré submarine volcano (Mayotte, Comoros archipelago)”, *Volcanica*, 9(2). doi: 10.30909/vol/irun2647.

Chalcogen element (S – Se – Te) constraints on the source of the Fani Maoré submarine volcano (Mayotte, Comoros archipelago)

I. Vlastélic[1,2,*], J.-L. Piro[1], V. Famin[2,3], C. Berthod[2], P. Bachèlery[1], T. Rouyer[1], A. Di Muro[4]

[1] Université Clermont Auvergne, CNRS, IRD, OPGC, Laboratoire Magmas et Volcans, F-63000 Clermont-Ferrand, France

[2] Université Paris-Cité, Institut de physique du globe de Paris, CNRS, UMR 7154, F-75005 Paris, France

[3] Université de La Réunion, Laboratoire GéoSciences Réunion, F-97744 Saint-Denis, France

[4] Laboratoire de Géologie de Lyon Terre - Planètes – Environnement, Observatoire de Lyon, UAR 3721 COMET

[*] ivan.vlastelic@uca.fr [corresponding author]

ORCiD (IV): 0000-0002-6701-4832
ORCiD (VF): 0000-0001-7451-5363
ORCiD (CB): 0000-0001-6890-5541
ORCiD (PB): 0000-0002-0108-5486
ORCiD (ADM):

Keywords: Sulfur, selenium, tellurium, sulfide, magma degassing, mantle source

Article in press

Abstract

Between 2018 and 2020, the Fani Maoré eruption produced approximately 6.5 km^3 of CO_2-rich basanite offshore Mayotte Island. This event raises the question of the formation, storage and destabilization of large volumes of magma in the Comoros lithospheric mantle. In particular, the content, origin and role of volatile elements carbon and sulfur in the magma source is a matter of debate. This issue is investigated here by examining chalcogen elements sulfur (S), selenium (Se), and tellurium (Te) which are retained in Fani Maoré sulfide-saturated lavas. Compared to submarine basalts produced by mid-ocean ridge, hotspot or arc volcanism, Fani Maoré lavas are depleted in Se (66–81 ppb) and enriched in Te (4.4–13.6 ppb), and display unusually high S/Se (up to 22,130) and low Se/Te ratios (down to 5.1). The high-Te low-Se/Te signature is best explained by addition of 0.015-0.03 wt% Te-rich metasomatic sulfides in the magma source, consistent with previous models of Comoros volcanism. Sulfide saturation during magma differentiation only partially accounts for the high S/Se ratio of lavas. Instead, the observation that Fani Maoré lavas plot at the upper end of the global correlation between S/Se and Sm/Yb ratios suggests that the high S/Se signature of Fani Maoré primarily reflects the partitioning of Se in mantle residual sulfides relative to carbonated silicate melts during incipient melting in the garnet stability field. The presence of small amounts (0.035- 0.085 wt%) of Se-poor sulfates recycled into Fani Maoré magma source could also explain the high S/Se ratios, but this contribution is not essential. The sulfide deposits in Tanzania are also characterised by particularly high S/Se ratios, reinforcing the view that the magmatism in the Comoros and that of the East African Rift share a similar origin.

Article in press

1 Introduction

The Comoros Archipelago is the subaerial expression of a series of volcanic ridges located in the Mozambique Channel between Africa and Madagascar (Figure 1a). The origin of Comoros volcanism has long been debated and may be related either to the interaction of a deep mantle plume with the oceanic lithosphere (Hajash and Armstrong, 1972; Emerick and Duncan, 1982; Class et al., 1998, 2005) or to a regional trans-tensional tectonic regime linked to the East African Rift System (Nougier et al., 1986; Michon, 2016; Famin et al., 2020). In both cases, the unusual geochemistry of Comoros lavas (e.g. elevated CaO content and K-Ba negative anomalies indicative of the presence amphibole in the magma source) suggests partial melting of a lithosphere metasomatized by volatile-rich fluids or melts (Class and Goldstein, 1997; Pelleter et al., 2014).

Between 2018 and 2020, a submarine eruption produced ~6.5 km^3 of basanite 55 km east of the Mayotte Island, the easternmost island of the archipelago, and recently revived the debate on the origin of Comoros volcanism (Feuillet et al., 2021; Thinon et al., 2022; Berthod et al. 2021, 2022). Magma degassing resulted in elevated concentrations of CO_2 (34 μM) in the water column (Feuillet et al., 2021) and, after the eruption, a major CO_2 hydrates field at the seafloor (Cathalot et al. 2026). The Sr-Nd-Pb isotopic composition of the new volcano, named Fani Maoré, supports a close genetic link with the Comoros mantle source (Chauvel et al., 2024). However, Fani Maoré lavas display unusual Ba enrichment and Pb depletion compared to both Comoros lavas and Ocean Island Basalts (OIB) more generally. This led Chauvel et al. (2024) to propose that Fani Maoré lavas derive from a mantle source enriched in Ba, CO_2 and sulfur.

This work further investigates the complex origin of Comoros volcanism using the chalcogen elements sulfur (S), selenium (Se), and tellurium (Te). These elements are volatile during subaerial eruptions (Greenland and Aruscavage, 1986; Mason et al., 2021; Zelenski et al., 2021), but are likely retained in the deep (>3 km) sulfide bearing pillow lavas of the Fani Maoré eruption (Berthod et al. 2021), as observed in sulfide saturated Mid-Ocean Ridge Basalts (MORB; e.g., Lissner et al., 2014, Yierpan et al. 2019). Like S, Se and Te occur in nature with oxidation states of -2, +4, and +6. However, Se-S and Te-S substitutions are redox-dependent: unlike the +4 and +6 species, S^{2-}, Se^{2-}, and Te^{2-} have very similar ionic radii (Shannon et al., 1976), allowing extensive substitution in reducing conditions only. Selenium and tellurium are thus incompatible in sulfate, but compatible in sulfide, with Sulfide Liquid (SL) –Silicate Melt (SM) partition coefficients ($K^{SL/SM}$) of several hundred for Se and several thousand for Te (Helmy et al., 2010; Patten et al., 2013; Brenan, 2015; Kiseeva et al., 2017; Liu and Li, 2025). Because selenium is less volatile than sulfur at atmospheric pressure, Se can be used to reconstruct the behaviour of S in magmatic systems from partially degassed lavas (Jenner et al., 2010). The Se–Te element pair is also useful

Article in press

for tracking the evolution of sulfide melt during magma cooling and crystallization, because of the large Se/Te fractionation between coexisting sulfide liquid and Monosulfide Solid Solution (MSS; Helmy et al., 2010; Brenan, 2015). Using high-precision isotope dilution measurements of S, Se, and Te, this work shows that magmas from the Fani Maoré volcano display among the highest S/Se and lowest Se/Te ratios observed in oceanic volcanism. The petrogenetic processes able to modify these ratios are reviewed, and the implications regarding the Fani Maoré magma source are discussed.

2 The Fani Maoré eruption

Between 2018 and 2020, a new submarine volcanic edifice grew at the eastern end of the East Mayotte volcanic chain (EMVC), 55 km offshore Mayotte Island (Figure 1b). By October 2020, the volcano had risen to 820 m above the 3300 m-deep seafloor, and its volume was estimated at ~6.5 km^3 (Feuillet et al., 2021). The eruption was fed by a large (≥10 km^3) magma reservoir located in the lithospheric mantle (37-48 km depth) where primary melts evolved to a basanitic composition through 50% crystallization of a mineral assemblage consisting of 80% clinopyroxene and 20% olivine (Berthod et al., 2021). This reservoir may be connected to an even larger magmatic reservoir (more than 200 km^3) recently imaged at 23 ± 1 km below sea level beneath Mayotte Island (Wawrzyniak et al., 2025). The strong fractionation of Rare Earth Elements (REE) in Fani Maoré lavas, with Sm/Yb ~ 6.0–6.5, indicates that the primary melts were generated by a low degree of partial melting (~4 %) of a garnet-spinel lherzolite at depths of 80–100 km (Berthod et al., 2021).

During the Fani Maoré eruption, the magma production rate decreased from 150–200 m^3/s during the first year, to 70–80 m^3/s between May and July 2019, and to less than 35–45 m^3/s after August 2019 (ReVoSiMa, 2021). Consistent with this trend, Berthod et al. (2022) identified three main eruptive phases based on lava chemistry. From June 2018 to May 2019 (Phase 1), magmas ascended directly from the 37-48 km deep mantle reservoir and built the main edifice. Phase 1 magmas are the least evolved, with 4.0–5.0 wt% MgO. Between May and July 2019 (Phase 2), magmas followed a different path in the mantle, mixed with tephri-phonolitic magma stored at the base of the crust, and reached the surface on the southwestern flank of the volcano. Phase 2 magmas are more evolved, with 3.6–4.3 wt% MgO. Between August 2019 and January 2021 (Phase 3), magmas followed a different pathway within the crust, shifting the eruption site ~6 km northwest of the main edifice. Phase 3 magmas are more degassed due to the longer ascent pathway (Verdurme et al., 2024). During Phase 3 (October 2020), the MgO content of lavas increased from 3.6–4.0 wt% to 4.2–4.5 wt%, reflecting the exhaustion of the tephri-phonolitic magmas stored

Article in press

in the shallower reservoir. This evolution led Berthod et al. (2022) to distinguish the periods before (Phase 3a) and after (Phase 3b) October 2020.

3 Samples

The Fani Maoré samples selected for this study are fresh submarine lavas previously studied by Berthod et al. (2021, 2022) and Chauvel et al. (2024). The samples were dredged during the MAYOBS (Rinnert et al., 2019) and GEOFLAMME (Rinnert et al., 2021) cruises at depths ranging from 2,935 to 3,239 m (Table 1 and Figure 1b). Eight samples were selected to cover the three main phases of the 2018–2020 submarine eruption (Table 1). Except for one sample with 9.9 wt% MgO (MAY04-DR11-0704), all samples are basanites with limited compositional variability ($3.8 \leq MgO \leq 4.8$ wt%). The samples are gas-rich "popping rocks", with bulk porosity decreasing from 30–45% during Phase 1 to 5–20% during Phase 3 (Verdurme et al., 2024). Sulfide droplets occur in all these samples and are most abundant in the Phase 3 samples (Berthod et al., 2022). To evaluate the extent of chalcogen degassing during lava emplacement and cooling, we also analysed nine subsamples drilled at regular intervals from the glassy margin to the core of a pillow lava (Figure 2). This lava erupted during the Phase 3 of the 2018–2020 eruption (sample GFL-DR20-0101 in Berthod et al., 2022, with 4.45 wt% MgO).

4 Analytical methods

All analyses were performed on rock powders obtained by crushing rock chips in an agate mortar. Except for the nine subsamples drilled across a pillow, chemical analyses were performed on powder representative of whole pillow (pillow interior plus glassy rim). The crushing procedure is considered to result in a homogenous distribution of the sulfide grains within the powder—at a scale much finer than the sample taken for analysis—thereby avoiding the "nugget effect". Selenium and tellurium concentrations were analysed by isotope dilution (ID) hydride generation (HG) quadrupole inductively coupled plasma mass spectrometry (ICP-MS, Agilent 7500, Laboratoire Magmas et Volcans) following a method modified from Yierpan et al. (2018). We first prepared ^{77}Se-enriched (44.773 ppb Se with 94.38% ^{77}Se) and ^{125}Te-enriched (5.214 ppb Te with 95.52% ^{125}Te) spike solutions from solid sources obtained from Oak Ridge National Laboratory (USA). The concentrations of the spike solutions were calibrated by isotope dilution against solutions prepared by diluting a 10 µg/g certified standards (Inorganic Venture manufacturer). Spikes concentrations were obtained by averaging measurements of three spike-standard mixtures prepared close to the optimal spike/standard ratio. For sample analysis, 200 mg of rock powder was weighted in 15 ml Teflon vials. Immediately afterwards, we added 250–500 mg of ^{77}Se-enriched spike and 150–300 mg of ^{125}Te-

Article in press

enriched spike. Silicates were digested by sequential addition of 1 ml of 14M HNO_3 and 6 ml of 29M HF, and the vials were heated on a hotplate at 90°C for 24 h. Samples were evaporated at 70°C to avoid Se and Te volatilization (Vlastélic and Piro, 2022). The dry residues were taken in 3 ml of 6M HCl, heated at 90°C for 24 h, and evaporated at 70°C. This HCl conversion step was repeated once.

The two-step chemistry from Yierpan et al. (2018) was used to purify Se and Te. The column separation was calibrated by dissolving 320 mg of a La Réunion basalt doped with 500 ng of Se and Te. After HCl conversion, the sample residues were dissolved in 3 ml of 4M HCl, centrifuged for 5 min, and loaded on anionic columns (polypropylene Biorad filled with 5 ml of AG1-X8 100–200 mesh resin). Most elements and Se were eluted by successive additions of 3 ×1 ml and 4 ml of 4M HCl, while Te was retained, probably as chloro-complex. Iron was eluted with 2 × 5 ml of 2M HCl – 5M HF acid mixture followed by 2 × 3 ml of 0.4M HCl. Tellurium, together with minor amounts of remaining Pb, was then eluted with 6 ml of 0.4M HCl. After evaporation at 65°C, the major element–Se fraction was dissolved in 4 ml of 0.1M HNO_3, centrifugated, and loaded on cationic columns (polypropylene Biorad filled with 5 ml of AG50-X8 200–400 mesh resin). Selenium was eluted by successive additions of 2 × 1 ml and 3 ml of 0.1M HNO_3. Although the collected Se fraction is not highly pure, it is sufficiently depleted in Fe and other transition metals to allow efficient hydride generation during subsequent ICP-MS analysis. Recovery of ~70% and >90% were estimated for Se and Te chemical separation, respectively. After evaporation at 85°C, the fractions of Se (0.14–135 ng) and Te (0.04–24 ng) recovered from samples were taken up in 6 and 3 ml of 1M HNO_3, respectively. The resulting solutions (0.02–23 ppb Se and 0.013–8 ppb Te) were mixed online with 0.3M $NaBH_4$ in 0.1M NaOH in a hydride generation system (HGX-200 from Teledyne Cetac Technologies). The H_2Te and H_2Se vapours were entrained by two Ar flows (carrier flow of 0.42 L/min and make up flow of 0.82 L/min) to an Agilent 7500 ICP–MS. To improve ICP-MS sensitivity, we used two primary pumps increasing the vacuum of the interface. $^{78}Se/^{77}Se$ was measured using the reaction cell (He mode) to lower polyatomic interferences from the Ar carrier gas (e.g., $^{40}Ar^{38}Ar^+$, $^{36}Ar^{40}Ar^1H^+$, $^{38}Ar_2{}^1H^+$), while $^{126}Te/^{125}Te$ was measured in "no-gas" mode. Each measurement included typically 100 scans, with 200 ms acquisition on each mass, for a total acquisition time of ~1 min. The 1M HNO_3 solution used to dissolve samples was repeatedly measured for background correction. Instrumental mass fractionation was corrected by measuring a 5 ppb Se isotopic standard (NIST SRM 3149) and a 1 ppb Te isotopic standard (NIST SRM 3156) at the beginning and/or end of each session. Signals of ca. 130,000 CPS/ppb ^{78}Se and 500,000 CPS/ppb ^{126}Te were measured on the NIST SRM solutions.

Sulfur concentrations were measured by isotope dilution using a ^{34}S-enriched spike (262 ppm S, with 99.79% ^{34}S). The spike, initially in the form of native sulfur, was dissolved in 14M HNO_3 and calibrated against IAEA-S-1 sulfur isotope reference material. For sample analysis, 50 mg of rock powder was weighted into 15 ml Teflon vials, spiked

Article in press

and digested with 1 ml of 14M HNO_3 and 6 ml of 29M HF at 90°C for 24 hours. After evaporation, the fluoride residue was reduced by addition and evaporation of a few drops of 14M HNO_3. Unlike the procedure of Wang and Becker (2013), sulfur was not separated because of significant S release (>1 μg) from the cationic resin. Instead, the residue was taken in 5 ml of H_2O, centrifugated, and the $^{32}S/^{34}S$ ratio of the supernatant was directly analysed on an Element XR ICP–MS in high mass-resolution mode (m/Δm of 10 000). To verify the accuracy of S isotope compositions, the $^{32}S/^{34}S$ ratios of a subset of samples from Fani Maoré volcano were also measured as oxides ($^{32}S^{16}O/^{34}S^{16}O$), using the oxygen reactive mode of an Agilent 8900 triple quadrupole ICP–MS. Instrumental mass fractionation was corrected by running IAEA-S-1 sulfur isotope reference material. Sample concentration (C_{Sample}) was calculated according to:

$$C_{Sample} = C_{Spike} \times \frac{m_{Spike}}{m_{Sample}} \times \frac{Ab^{B}_{Spike}}{Ab^{B}_{Sample}} \times \frac{R_{Spike} - R_{mes}}{R_{mes} - R_{Sample}} \quad \text{(Eq. 1)}$$

Where C_{spike} is the spike concentration, m_{spike} and m_{sample} are the spike and sample masses, R_{spike}, R_{sample}, and R_{mes} are the isotopic ratios of the spike, the sample, and the measured sample-spike mixture, respectively. As R_{sample} is not measured, we use the natural abundances of Se and Te isotopes of the NIST standards. Ab^{B} is the isotopic abundance of the denominator isotope. The precision of isotopic ratios measured by ICP–MS is typically on the order of 1–3 %. The precision of concentrations obtained by isotope dilution is inferred from the error magnification (M), defined as:

$$M = \frac{\Delta C_{Sample}}{C_{Sample}} \Big/ \frac{\Delta R_{mes}}{R_{mes}} = \frac{R_{mes} \cdot (R_{Spike} - R_{Sample})}{(R_{Spike} - R_{mes}) \cdot (R_{mes} - R_{Sample})} \quad \text{(Eq. 2)}$$

Error magnification ranges between 1.03 and 1.3. Average procedural blanks are 0.8 ng S, 0.2 ng Se and 0.05 ng Te. The concentrations of the four reference basalts measured during this study (BHVO-2, BCR-2, BEN, and BIR-1, Table 1) fall within the range of the recommended values reported in the GeoRem database (Jochum et al. 2005). However, our S value of BIR-1 (4.4 ppm) is much lower than the information value of 70 ppm reported in the database. The concentrations of conventional trace elements in drilled subsamples were analysed by ICP-MS using the method described in Vlastélic et al. (2013). Data obtained for international reference materials with this method are provided in supplementary Table S1.

Article in press

5 Results

Sulfur, selenium and tellurium concentrations in the Fani Maoré samples are reported in Table 1, together with published MgO, $Fe_2O_{3(T)}$ and Cu data (Berthod et al., 2022; Chauvel et al., 2024). Complementary trace element data of the nine subsamples drilled in GFL-DR20-0101 are reported in supplementary Table S1.

5.1 Chalcogen and Cu composition of lavas from the Fani Maoré submarine eruption

Fani Maoré lavas contain between 1342 and 1711 ppm sulfur and plot on, or slightly below, the sulfide-saturated MORB array in the S versus $FeO_{(T)}$ diagram (Figure 3), consistent with the occurrence of iron sulfide droplets in all samples (Berthod et al., 2021). In Figure 4, chalcogen elements together with less volatile Cu are plotted against the MgO content of the lavas and compared with worldwide MORB, hotspots, and oceanic plateau volcanic glasses. This comparison reveals that Fani Maoré evolved basanites (i.e., with MgO between 3.8 and 4.8 wt%) have lower Se (66–81 ppb) and Cu (15.9–27.1 ppm) contents than most oceanic lavas of similar MgO content (Figure 4b-c). Such depletion in Se and Cu is only observed in a few lavas from Samoa and in subaerial lavas from the nearby Mayotte Island (for Cu only). Fani Maoré lavas show S/Se (16929–22130) and S/Cu ratios (50–95) at the upper limit of oceanic basalts range, but intermediate Cu/Se ratios (233–336) close to the average value of oceanic basalts (Figure 4e-g). Unlike Se and Cu, Te is enriched in Fani Maoré lavas (4.4–13.6 ppb) compared to similarly evolved MORB and arc lavas, a feature also observed in some samples from Loihi (Hawaii) (Figure 4d). The combination of low Se and high Te contents in Fani Maoré lavas results in some of the lowest Se/Te ratios reported for oceanic volcanism (5.14–15.6; Figure 4h).

The more magnesian sample (9.9 wt% MgO; MAY04-DR11-0704) has S, Se, and Te concentrations similar to those of the evolved basanites, but a higher Cu content (106 ppm), which nevertheless falls in the range of Mayotte Island lavas with ca. 10% wt% MgO (Figure 4c). Within the small MgO range of Fani Maoré evolved basanites, S generally increases, whereas Se and Cu generally decrease with decreasing MgO. Tellurium remains relatively constant (4.4–6.1 ppb) in samples with > 3.9 wt% MgO, but increases markedly (9.5–13.6 ppb) in the most evolved samples, yielding very low Se/Te ratios (5.1–7.2).

5.2 Radial zonation of chalcogens in a pillow lava

The selected pillow lava (GFL-DR20-0101) displays five concentric layers with distinct textures (Figure 2). In the core of the pillow (Layer 1), only rare, small (< 1 mm), rounded vesicles occur. The overlying thick Layer 2 is

Article in press

characterised by the presence of 1-3 cm pipe vesicles with a radial distribution. The abundance of pipe vesicles markedly increases in Layer 3. However, closer to the surface, where the extent of crystallization decreases, neither vesicles nor degassing pipes occur in Layers 4, 5, and 6. Layer 5 stands out from Layer 4 by the presence of glass, whereas the pillow rim (Layer 6) is entirely glassy. This texture is very similar to that described by Berthod et al. (2022) for a pillow lava erupted earlier during the eruption. More generally, this degassing-crystallization structure is typical of pillows lavas (e.g., Philpotts and Lewis, 1987; Merle et al., 2005).

Variations in S, Se, Cu, and Te concentrations, as well as S/Se, S/Cu, Cu/Se, and Se/Te ratios from the pillow rim to the core are reported in Figure 5. Sulfur and Se display similar variations, with the base of Layer 2 being depleted in S (1,518–1,593 ppm) and Se (76.8–77.0 ppb) relative to both the pillow core (1,671–1,794 ppm S and 82.6–83.5 ppb Se) and the outer layers (1,751–1,881 ppm S and 82.1–83.6 ppb Se). Sulfur being more depleted than Se in Layer 2, S/Se ratios are lower in this layer (19,706–20,738) than in the pillow core (20,235–21,496) and the outer layers (21,243–22,641). Copper concentrations (21.2–24.3 ppm) vary barely outside analytical error, although slightly higher values (>23 ppm) may occur at the base of Layer 3 and the top of Layer 2 relative to the rest of the pillow. Consequently, S/Cu ratios vary as S, with lower values (68–69) in the middle of the pillow compared to the core and external layers (81–83). The Cu/Se ratio displays limited variations, with slightly higher values (281–296) at the base of Layer 3 and the top of Layer 2 compared to the rest of the pillow (264–275). Tellurium exhibits a different zonation pattern, with low and homogeneous concentrations (4.5–4.9 ppb) in the internal layers 1-2, and markedly higher concentrations (5.7–6.0 ppb) in the outer layers 3-6. Consequently, Se/Te ratios are lower in the outer layers (13.8–14.7) than in the internal layers (16.3–17.2). In contrast, the concentration of refractory lithophile elements remains constant within analytical error (~5 %) across the pillow lava (supplementary Table S1).

6 Discussion

Following a top-down approach, the discussion successively evaluates how magma degassing, magma differentiation, partial melting, and composition of the mantle source can explain the extreme chalcogen element signature of Fani Maoré lavas.

6.1 Chalcogens degassing during submarine lavas emplacement

Volatile elements being highly incompatible in silicate minerals, cooling and crystallization of magmas drive an increase in the volatile concentration in the residual melt, and ultimately the exsolution of a volatile phase. This

Article in press

process known as “second boiling” in magma chamber, is critical when erupted lavas solidify at the surface. The extent of lava solidification driven degassing remains limited in deep-ocean setting where the hydrostatic pressure prevents the exsolution of water and sulfur, and/or when stable sulfides retain chalcophile elements. The sulfide-saturated nature of Fani Maoré lavas (Figure 3) is testament to minimal loss of S and chalcogen elements, because sulfur outgassing would induce sulfide breakdown (Edmonds and Mather, 2017). Nevertheless, measurable chalcogen degassing can occur during the cooling of sulfide-saturated pillow lavas (Lissner et al., 2014; Forrest et al., 2017; Yierpan et al., 2021; this work). For instance, Forrest et al. (2017), in their study of Reykjanes ridge basalts, noted that sulfur concentrations are generally lower in the crystallised cores of pillow lavas than in the glassy rims, whereas the difference is less systematic for Se, and especially for Te. This issue must be first evaluated because the S-Se-Te analyses were performed on powder representative of whole pillow.

The radial zonation of the studied pillow (Figure 5) reveals that S and Se are significantly degassed at intermediate depth within the pillow, where pipe vesicles occur, whereas Te is depleted throughout the pillow interior. We use this zonation to quantitatively assess chalcogen element degassing at the scale of an individual pillow and to evaluate the effect of chalcogens degassing on the bulk composition data reported in this study. To this end, the sample was divided into nine sections (s) corresponding to the nine analyses. The boundaries between sections were set as the midpoints between adjacent drill holes (Figure 2). The volume of each section (V_S) was calculated assuming a spherical geometry and a uniform density. At the scale of the pillow, the mass fraction of an element lost by degassing (ε) is calculated according to (Eq. 3) (Rubin, 1997):

$$\varepsilon_x = 1 - \frac{C_f}{C_i} = 1 - \frac{\sum_{s=1}^{s=9} C_S \times V_S / V_{Pillow}}{C_i} \quad \text{(Eq. 3)}$$

Where C_i and C_f are the bulk concentrations of the pillow lava before and after cooling, respectively. C_i is assumed to be equal to the highest concentration measured in the pillow lava, generally occurring in or near the glassy rim, whereas C_f is calculated by integrating the amount of element in each section ($C_S.V_S$). At the scale of the whole pillow, ε is estimated to be 6.5% for S, 7.2% for Te, and only 1.6% for Se, confirming the lower volatility of Se during lava emplacement. Using these values, the S/Se and Se/Te ratios of the bulk pillow are estimated to be ~5% lower and ~6% higher than magmatic ratios, respectively (i.e., S/Se slightly decreases, whereas Se/Te slightly increases during pillow lava degassing). These results indicate that the elevated S/Se ratios measured in Fani Maoré lava rocks represent minimum estimates of the pre-emplacement magma, whereas the low Se/Te ratio represent maximum estimates. This further emphasises the extreme chalcogen signature of Fani Maoré magmas.

Article in press

290

6.2 Sulfide fractionation during magma differentiation

Mantle-derived magmas evolve towards sulfide saturation during their differentiation in crustal reservoirs due to crystallization of S-free silicate minerals which increases S concentration in the residual melt (Edmonds and Mather, 2017) and late-stage magnetite crystallization which reduces the sulfur concentration at sulfide saturation (SCSS) (Jenner et al., 2010). Previous works (e.g. Lissner et al., 2014; Yierpan et al., 2019; Wieser et al., 2020; Liu and Li, 2025) showed that segregation of dense, immiscible sulfide liquid with >30 wt% S, $K_{Se}^{SL/SM}$ and $K_{Te}^{SL/SM}$ in the range of 10^2-10^3 and 10^3-10^4, respectively (e.g., Patten et al., 2013; Brenan, 2015; Kiseeva et al., 2017; Liu and Li, 2025) drives an increase of S/Se and Se/Te ratios in the residual magma during differentiation of MORB and OIB. In evolved MORB (5–6 wt% MgO) the cooler sulfide phase contains some Monosulfide Solid Solution (MSS) fractionating Se and Te in the opposite direction (Helmy et al., 2010; Brenan, 2015; Yierpan et al., 2019). Compared to other oceanic basalts, Fani Maoré lavas except sample MAY04-DR11-0704 display lower Cu content at given MgO (Figure 4c), which is indicative of significant sulfide fractionation. The differentiation temperatures of Fani Maoré magmas (1095–1075°C for the main stage and 1024 ± 50 ◦C for evolved magmas; Berthod et al., 2021; Wawrzyniak et al., 2025) being similar or below sulfide solidus at corresponding depths (1134-1109°C for main stage and 1061°C for evolved magmas, Zhang and Hirschmann (2016)) the segregating sulfide is likely mostly crystalline. Constraints on the nature of the segregating sulfide may also be inferred from the magnesian sample MAY04-DR11-0704. This sample has elevated CaO (11.4 wt%), Cr (411 ppm), V (263 ppm), Ni (221 ppm) and Sc (24.5 ppm), compared to other Fani Maoré lavas (CaO < 7.2 wt%, Cr < 86 ppm, V < 162 ppm, Ni < 58 ppm and Sc <18 ppm) likely due to the entrainment, and possible dissolution upon fast decompression (Brearley and Scarfe, 1986), of a clinopyroxene-rich magma chamber cumulates, similar to the 0.8 Cpx-0.2 Ol dominant fractionating mineral assemblage (Berthod et al., 2021). Compared to Fani Maoré lavas with less than 5 wt% MgO (Figure 4), MAY04-DR11-0704 sample has much higher Cu content (106 ppm), but similar S, Se and Te contents. This suggests that the cumulative phase has elevated Cu/S, Cu/Se and Cu/Te relative to Fani Maoré magmas. Providing that the entrained cumulate is representative of the bulk fractionating phase, segregation of Cu-rich crystalline sulfide might dominate in Fani Maoré magmatic system. Fractionation of Cu-rich (25-58 wt.%) crystalline sulfide has previously been shown below 1100°C in arc and hotspot magmas (e.g. Jenner et al., 2010; Greaney et al., 2017). In the following, sulfide fractionation is estimated quantitatively, with the aim of constraining the composition of Fani Maoré parental magmas. Mantle derived magma is assumed to have 1,200 ppm S, as estimated for deep CO_2-bearing melts saturated in sulfide (Fux et al., 2025), and 106 ppm Cu as Mg-rich lavas from Mayotte island (Pelleter et al. 2014). This magma is expected to evolve away from sulfide saturation during ascent, due to the increase in

Article in press

SCSS with decreasing pressure, and to become sulfide-saturated again during magma differentiation (Edmonds and Mather, 2017). It is estimated that 0.16% segregation of sulfide with 30 wt% S and $K_{Cu}^{Sulfide/SM}$=1,000 during 50% crystallization of 0.8 Cpx-0.2 Ol (with $K_{Cu}^{Ol/SM}$=0.1 and $K_{Cu}^{Cpx/SM}$=0.21 from Greaney et al. (2017)) is required to increase S up to 1440 ppm while decreasing Cu below 22 ppm in the residual magma (average of Fani Maoré lavas except the two most evolved samples and the magnesian sample MAY04-DR11-0704). The fractionating phase assemblage contains 0.32% sulfide (=0.16/50). The decrease in Cu/Se with decreasing MgO content (Figure 4g) requires $K_{Se}^{Sulfide/SM} < K_{Cu}^{Sulfide/SM}$. Using $K_{Se}^{Sulfide/SM}$=450 consistent with the Fe-rich composition of Fani Maoré magmas (Kiseeva et al., 2017; Liu and Li, 2025), 95 ppb Se is estimated for the parental melts (S/Se=12,632). Given the incompatibility of Te in crystalline sulfide (Helmy et al., 2010; Brenan, 2015) and the uniform Se/Te in Fani Maoré lavas (except the two most evolved samples, Figure 4g) we assume $K_{Te}^{Sulfide/SM} = K_{Se}^{Sulfide/SM}$, yielding 7.0 ppb in the parental melt (Se/Te= 13.6). In summary, although sulfide segregation substantially fractionates S from Se and Te in the residual magma, the S/Se and Se/Te ratios estimated for Fani Maoré parental melts remain significantly higher and lower, respectively, than most oceanic basalts.

6.3 Melting processes

Fani Maoré magmas were generated by a low degree of partial melting (~ 4%) of a garnet-spinel lherzolitic source at 80–100 km depth (Berthod et al., 2021), well below the lithosphere-asthenosphere boundary, which lies at ~65 km below sea level (Dofal et al., 2023). The Si-undersaturated nature of Fani Maoré basanites also requires the contribution of even deeper (>150 km) CO_2-rich melts produced by "redox melting" (e.g., Fux et al., 2025). The S-Se-Te composition of mantle derived melts is modelled in Figure 6 and compared to the composition estimated above for Fani Maoré parent melt. A near-fractional melting model (e.g., Rehkämper et al., 1999) is used where sulfide liquid (SL) is the main phase bearing sulfur in Fani Maoré mantle source. Sulfur solubility in silicate melt is set at 1200 ppm as estimated for deep carbonated melts saturated in sulfide (Fux et al., 2025). We use Se and Te partition coefficients determined for iron-rich silicate melts equilibrated with sulfide liquid between 0.5 and 2.5 GPa ($K_{Se}^{SL/SM}$=200 and $K_{Te}^{SL/SM}$=1,500, from Liu and Li, (2025)), and for carbonated silicate melts (CSM) equilibrated with sulfide liquid at 5 GPa ($K_{Se}^{SL/CSM}$ = 914 and $K_{Te}^{SL/CSM}$=5,906, from Fux et al. (2025)). The difference in Se-Te partitioning is consistent with Chowdhury et al. (2021) who found that the partition coefficients of chalcophile elements (Co, Ni and Mo) between sulfide and carbonated silicate melts are higher than the partition coefficients of these elements between sulfide and silicate melt. Conversely, it disagrees with Xue and Li (2025) who found low $K_{Se}^{SL/CSM}$ (42 – 98) in experiments conducted at 1-3 GPa.

Article in press

Figure 6 shows modelled primary magma compositions as a function of the degree of melting. Low-degree melting of a fertile mantle with bulk silicate earth (BSE) composition produces melts with high Se and Se/Te, and low Te and S/Se compared to Fani Maoré parent melt for either of the two BSE compositions used for the source (211 ppm S, 80 ppb Se and 11 ppb Te according to Wang and Becker (2013) or 250 ppm S, 25 ppb Se and 1.37 ppb Te according to Liu and Li (2025)). The same observation holds also true when considering a depleted MORB mantle (DMM) with 185 ppm S, 49 ppb Se and 3.5 ppb Te (Yierpan et al., 2019). In the following, mantle composition is adjusted to reproduce the composition of Fani Maoré parental magma at $F_{melting}$=4%. This adjustment is carried out by varying the S and Te contents of the source while keeping Se concentration in the 25-80 ppb range proposed for the BSE and DMM (Wang and Becker, 2013; Yierpan et al., 2019; Liu and Li, 2025). This approach is based on the anomalous behaviour of S and Te, relative to Se, in mantle peridotites (Lorand and Alard, 2010; König et al. 2014). Three successful combinations of source composition and K_d are shown on Figure 6. For $K_{Se,Te}^{SL/SM}$ and Se_{mantle}=25 ppb from Liu and Li (2025), the composition of Fani Maoré parental melt is best explained by melting of a source containing 450 ppm S and 13 ppb Te (S/Se=18,000 and Se/Te=1.9). With $K_{Se,Te}^{CSL/SM}$ from Fux et al. (2025), the mantle source must have 185 ppm S and 18 ppb Te (S/Se=4,625 and Se/Te=2.2) for Se_{mantle}=40 ppb, and 350 ppm S and 38 ppb Te (S/Se=4,375 and Se/Te=2.1) for Se_{mantle}=80 ppb. In summary, model results systematically indicate a significant enrichment in Te in Fani Maoré magma source relative to the different estimates of the BSE and DMM, and a sulfur content that is identical or in slight excess.

6.4 Origin of the low Se/Te and high S/Se ratios of Fani Maoré magmas

Although Fani Maoré melts initially formed in the asthenospheric mantle (Berthod et al., 2021), partial melting of the extensively metasomatized Comoros lithosphere (Class and Goldstein, 1997; Pelleter et al., 2014) could contribute chalcogen elements. In support of this possibility, the high-Te low-Se/Te signature of Fani Maoré lavas is best explained by addition of Te-rich metasomatic sulfides in the magma source. Metasomatic sulfides are evolved phases precipitating from sulfide-bearing metasomatic fluids. Their composition is complementary to that of residual MSS (Alard et al., 2000; Luguet et al. 2004; König et al. 2014, 2015). Figure 7a shows that the Se-Te composition estimated in section 6.3 for Fani Maoré magma source can be explained by addition of 0.015-0.03 wt% of metasomatic sulfide with 121 ppm Te and 101 ppm Se (average of metasomatic sulfides from Luguet et al. (2004) and König et al. (2014)) to a mantle with chalcogen composition within the DMM-BSE range (Wang and Becker, 2013; Yierpan et al., 2019; Liu and Li, 2025). This content of metasomatic sulfide corresponds to the maximum observed in mantle peridotites (König et al. 2014).

Article in press

On the other hand, the high S/Se ratio estimated for Fani Maoré parental melts (S/Se=12,632) can be explained in different ways. We discuss below three hypotheses: (1) external S-rich lithologies in the Fani Maoré magma source; (2) the assimilation of S-rich sediments by mantle-derived magmas; and (3) partial melting conditions specific to the Comorian volcanism, without the need for an input of external sulfur.

Hypothesis (1): A first possible cause of the elevated S/Se signature is the occurrence of S-rich recycled components in the magma source. Sulfur enrichment relative to Se is characteristic of hydrothermal and sedimentary environments, where S/Se ratios are up to 5×10^4 in hydrothermal sulfides (Luguet et al., 2004), 3×10^5 in crustal pyrite of sedimentary origin (Lorand and Alard, 2011), and up to 10^7 in evaporitic sediments such as gypsum (Malisa, 2001). In agreement with this possibility, the Ba enrichment observed in Fani Maoré lavas has been attributed to the presence of ~0.005 wt% baryte ($BaSO_4$) of possible hydrothermal origin in the mantle source (Chauvel et al, 2024). Figure 7b shows that addition of 0.06 wt% anhydrite (or sulfate with similar molar mass) with S/Se of 10^7 to a fertile lherzolite with 80 ppb Se and 211 ppm S (BSE composition of Wang and Becker (2013)) reproduces Fani Maoré modelled source with 80 ppb Se and 350 ppm S (red square in Figure 7b). This process is labelled "1a" in Figure 7b. Slightly higher anhydrite contribution of 0.085 wt% is required to explain Fani Maoré modelled source (blue square in Figure 7b) from the BSE composition of Liu and Li (2025) (process labelled "1b" in Figure 7b). These estimates are not inconsistent with the conclusions of Chauvel et al (2024), considering that baryte is likely a minor fraction of total sulfate. More elaborate modeling consistent with Se-Te constraints (Figure 7a) should consider the presence of metasomatic sulfides with moderate S/Se ratios (between of 2,176 and 3,362 according to Luguet et al. (2004) and König et al. (2014)) in addition to high-S/Se recycled sulfate in the mantle source. It is estimated that addition of only 0.035 wt% anhydrite plus 0.03 wt% metasomatic sulfide (with 27.2 % S and 101 ppm Se) to a mantle with 185 ppm S and 49 ppb Se (DMM composition of Yierpan et al., 2019) can reproduce the modelled source with 350 ppm S and 80 ppb Se (red square). This is process is labelled "1c" in Figure 7b.

Hypothesis (2): The second hypothesis considers that mantle-derived magmas assimilate S-rich sediments or external sulfur trapped in the crust. Pyrite-rich Pyrenean peridotites with high S/Se ratios (Lorand and Alard, 2011) are an example of such contaminated lithosphere. The crustal contamination hypothesis could explain why the highest S/Se ratios (20,853 - 22,130) are observed in the most evolved lavas from eruption phase 2, which remobilized tephri-phonolitic magmas stored at the base of the crust (see Figure 12 of Berthod et al., 2022). As shown in Figure 7b, Fani Maoré parental melts can be modelled by assimilation of ~0.06 wt% crustal pyrite with S/Se=126,188 (Lorand and Alard, 2011), or ~0.15 wt% evaporite gypsum with S/Se=10^7 by a hypothetic primary melt with Se content as Fani Maoré parental melt (95 ppb) but significantly lower S (900 ppm). However, this

Article in press

possibility (hypothesis 2 in Figure 7b) remains difficult to reconcile with Sr isotope data, which indicate that sulfur cannot have a sedimentary origin if it comes from the baryte that is necessary to explain the large Ba positive anomaly of lavas (Chauvel et al., 2024).

Hypothesis (3): The third and most likely possibility is that the high S/Se signature directly results from low-degree melting of a mantle source with S (185 ppm) and Se (40 ppb) contents (green square in Figure 7b) within the range (170 - 200 ppm S and 49±11 ppb Se) proposed for the DMM by Yierpan et al. (2019) (hypothesis 3 in Figure 7b). Here, the high S/Se ratio results from the combination of (1) the strong partitioning of Se in mantle sulfide relative to carbonated silicate melts (Fux et al., 2025), leaving behind carbonated silicate melts depleted in Se and, (2) the low degree of melting of Fani Maoré mantle source (~4%, Berthod et al., 2021) which ensures that sulfide is not exhausted (Figure 6). In support of this possibility, S/Se correlates positively with Sm/Yb (a proxy for the depth of melting) in submarine oceanic basalts, with Fani Faoré lavas plotting at the upper end of the correlation (Figure 8) where CO_2-rich melts produced by "redox melting" at depth > 150 km (Fux et al., 2025) are the least diluted in peridotite and/or eclogite melts produced at shallower depth. This suggests that extraction of low-degree partial melts from great depths (hypothesis 3), coupled with sulfide fractionation during magma differentiation, are the major processes increasing the S/Se ratio of magmas. Recycling of external sulfates in Fani Maoré magma source (hypothesis 1) could contribute to the high-S/Se signature of lavas, although this contribution is not essential.

6.5 Relation with East African Rift magmatism

Chauvel et al, (2024) noted geochemical similarities between Fani Maoré and carbonated volcanism along the nearby East African Rift, suggesting a possible genetic link between the two systems. In the absence of relevant S-Se data for East African Rift lavas, which are subaerial and extensively degassed, this hypothesis can be evaluated here using the global compilation of S/Se ratios in sulfide deposits (Queffurus and Barnes, 2015). This dataset shows a wide range of S/Se ratios (~500 to ~40,000), with both positive and negative deviations from mantle values (2850–4350 in this work). Interestingly, the highest S/Se ratios (36,078–42,358) are reported from the Kabanga picrite-hosted Ni–Cu deposits in Tanzania (Figure 1a). These elevated values have been attributed to extensive S assimilation from sulfide-bearing metasedimentary country rocks (Maier and Barnes, 2010). It is possible that both Comoros and East African Rift magmatism involve interaction with, or melting of, S-rich sedimentary rocks, implying that such components may be widespread in the regional mantle. This aligns with the idea that the two systems ~2,000 km apart share a common source enriched in carbon and sulfur (see synthesis by Chauvel et al,

Article in press

2024). Alternatively, both magmatic systems could be fed by low degree partial melts carrying a high S/Se signature due to Se partitioning in mantle residual sulfides.

7 Conclusions

The recent eruption of a large amount of CO_2-rich magma ("popping rocks") offshore Mayotte Island has raised questions regarding the origin of this exceptional event and its relationship to Comoros volcanism. In this study, we addressed these questions using high-precision measurements of the chalcogen elements S, Se, and Te in bulk rock samples. Sulfur concentrations (1,342–1,711 ppm) plot on the sulfide-saturated MORB array in S versus FeO space indicating limited S degassing. We estimate that less than 1.6% Se, 6.5% S, and 7.2% Te were outgassed during lava emplacement on the seafloor. Compared with global MORB and submarine OIB with similar MgO content, Fani Maoré lavas are remarkably depleted in Se (66–81 ppb) and enriched in Te (4.4–13.6 ppb), which results in unusually high S/Se (16,929–22,130) and low Se/Te ratios (5.14–15.6). Tellurium enrichment and low Se/Te ratios require up to 0.03 wt% metasomatic sulfide in the magma source, in agreement with previous models invoking extensive mantle metasomatism in the Comoros region. On the other hand, the high S/Se ratios primarily result from sulfide segregation during magma differentiation and low-degree melting within the garnet stability field (>80 km), where Se strongly partitions in residual sulfides relative to carbonated silicate melts. The S/Se ratios corrected for the effects of mantle melting and sulfide saturation during magma differentiation allow, but do not require, the presence of a small amount of recycled sulfate (0.035 - 0.085 wt% anhydrite) in Fani Maoré mantle source. At global scale, magma enrichment in S relative to Se is most clearly documented in sulfide deposits from Tanzania, where it has been attributed to assimilation of S-rich sedimentary materials. This similarity suggests that Comoros volcanism and the East African Rift may share a common mantle source enriched in sulfur, in addition to carbon. Alternatively, both volcanic systems could be supplied by low-degree partial melts with high S/Se ratio due to Se retention in mantle residual sulfides.

Article in press

Author contributions

I.V. designed the study, coordinated the analyses and wrote the paper

J.-L.P. performed S, Se and Te analyses by isotopic dilution

V.F. contributed to data interpretation and to the writing of the paper

C.B. collected samples, contributed to data interpretation and to the writing of the paper

P.B. collected samples, contributed to data interpretation and to the writing of the paper

T.R. performed S, Se, and Te analyses by isotopic dilution

A.D.M. contributed to data interpretation and to the writing of the paper

475

Acknowledgements

Se and Te NIST Standard Reference Materials were obtained from S. König, and ^{34}S-enriched spike from P. Cartigny. F.E. Jenner is thanked for sharing data compilation for oceanic basalts. We are grateful to Captain, Officers, and crew members of the GEOFLAMME oceanographic cruise (CNFH; PI C. Cathalot, E. Rinnert, N. Feuillet, https://doi.org/10.17600/18001297) onboard the R/V Pourquoi Pas? (GENAVIR/IFREMER, SHOM). The GEOFLAMME oceanographic funded marine operations that benefited to this study and provided dredged samples. The research was financed by the Institut de Recherche pour le Développement, the French Government Laboratory of Excellence initiative n° ANR-10-LABX-0006, the Region Auvergne and the European Regional Development Fund. Thanks to K. Iacovino for handling the manuscript, and to C. Chauvel and two anonymous reviewers for constructive comments. This is Laboratory of Excellence ClerVolc contribution number 770.

480

485

Data availability

All data generated during this study are included in this published article (and its supplementary information files)

490

Figure captions

Figure 1. Location maps. (a) Relief map of the southwest Indian Ocean showing the location of the Comoros Archipelago, Mayotte Island, and the East African Rift System. Bathymetric data are from the GMRT Synthesis (Ryan et al., 2009). (b) Relief map of Mayotte Island, showing the locations of dredged samples from the Fani Maoré submarine eruption, which occurred between 2018 and 2020 approximately 50 km east of Mayotte, along the East-Mayotte submarine Volcanic Chain. Bathymetric data from Thinon et al. (2022).

495

Figure 2. Cross section of a pillow lava emplaced during phase 3 of the Fani Maoré eruption (sample GFL-DR20-0101). Drill holes are shown and numbered from the pillow interior (DR20-1) to the pillow rim (DR20-12). Sample DR20-Sp is a chip taken from the thin glassy layer at the surface of the pillow. The five main textural unit (Layers

500

Article in press

1–5) and the surface glassy layer (Layer 6) described in text are indicated. Because the outer Layers 4 and 5 are thinner than the other layers, three to four smaller drill holes were taken and combined within each layer.

Figure 3. Sulfur versus FeO_T plot. Fani Maoré compositions are shown together with those of MORB, OIB, oceanic plateau, arc, and back-arc volcanic glasses. Data source includes Jenner et al. (2010, 2015), Reekie et al. (2019), Kurzawa et al. (2019), Wieser et al. (2020), and unpublished MORB, Samoa, and Iceland data compiled by Jenner and Jennings (2025). The sulfide-saturated MORB array is shown after Jenner and Jennings (2025). The error in Fani Maoré sulfur data (1 SD, Table 1) is smaller than symbol size. Error bar reported for sample GFL-DR20-0101 from Fani Maoré phase 3b is ± 1 SD of the 9 drilled samples (Table 1).

Figure 4. Sulfur, Se, Cu, and Te concentrations and ratios (S/Se, S/Cu, Cu/Se, Se/Te) versus MgO. Error bars (± 1 SD) are shown for Fani Maoré data (Table 1) where larger than symbol size. MgO and Cu data are from Berthod et al. (2022) and Chauvel et al. (2024). Data from this study are shown together with literature data for MORB, OIB, oceanic plateau, arc, and back-arc glasses and whole rocks. Data source: Yi et al. (2000), Jenner et al. (2010, 2015), Pelleter et al. (2014), Lissner et al. (2014), Reekie et al. (2019), Greaney et al. (2017), Kurzawa et al. (2019), Yierpan et al. (2019, 2021), Wieser et al., (2020), and unpublished MORB, Samoa, and Iceland data compiled by Jenner and Jennings (2025).

Figure 5. Radial compositional zonation of pillow lava GFL-DR20-0101, emplaced during Phase 3 (October - December 2020) of the Fani Maoré eruption (Berthod et al., 2022). Vertical dashed lines delimit the major textural layers shown in Figure 2 and described in the text. Error bars (± 1 SD) are shown where larger than the symbol size. Concentration data and analytical errors are reported in Table 1.

Figure 6. Modelled evolution of Se and Te contents (a, b), and S/Se and Se/Te ratios (c, d) during mantle partial melting. Melt compositions are calculated using a near-fractional melting model with a columnar melting regime (Rehkämper et al., 1999). An incremental method is applied, in which 1% melt equilibrates with the residue at each step. At each 1% melting increment, newly generated melts are mixed with the accumulated melts from previous increments. The compositional evolution of melts is shown for mantle sources with bulk silicate earth (BSE) (Wang and Becker, 2013; Liu and Li, 2025) and depleted MORB mantle (DMM) (Yierpan et al., 2019) compositions (black lines). Model results are also shown for different source compositions adjusted to reproduce the composition of Fani Maoré parental melts (see text) at $F_{melting}$=4%. This adjustment is carried out by varying the S and Te

Article in press

contents of the source while keeping Se values in the 25-80 ppb range proposed for the BSE and DMM (Wang and Becker, 2013; Yierpan et al., 2019; Liu and Li, 2025). Partition coefficients relevant to sulfide liquid (SL) equilibrating with iron-rich silicate melts (SM) between 0.5 and 2.5 GPa ($K_{Se}^{SL/SM}$=200 and $K_{Te}^{SL/SM}$=1500, Liu and Li, (2025)) and with carbonated silicate melt (CSM) at 5 GPa ($K_{Se}^{SL/CSM}$ = 914 and $K_{Se}^{SL/CSM}$=5,906 from Fux et al. (2025)) are considered. The partition coefficients of Liu and Li (2025) are only combined with the derived BSE estimates by the same authors. S solubility is set at 1,200 ppm consistent with sulfur concentration at sulfide saturation (SCSS) of CO_2-bearing melts (Fux et al., 2025).

Figure 7. Model of Fani Maoré magma source. (a) Se/Te vs Te plot. Mixing lines are shown between different BSE and DMM sources (Wang and Becker, 2013; Yierpan et al., 2019; Liu and Li, 2025) and metasomatic sulfide with 121 ppm Te and 101 ppm Se (average of metasomatic sulfides from Luguet et al. (2004) and König et al., (2014)). Numbers along the mixing lines indicate the proportion (wt%) of metasomatic sulfide in the mixture. (b) S/Se vs Se plot showing our three proposed models accounting for the high-S/Se ratio of Fani Maoré parental melts. In model 1, Fani Maoré mantle source is assumed to contain recycled sulfates with high S/Se. Mixing lines between different BSE estimates (Wang and Becker (2013) in model 1a; Liu and Li (2025) in model 1b) and anhydrite (23.5 wt% S and S/Se=10^7) are shown, with numbers along the lines indicating the proportion (wt%) of anhydrite in the mixture. The blue and red arrows refer to the corresponding melting models shown in Figure 6. Also shown (model 1c) is the addition of anhydrite plus metasomatic sulfides (with 27.2 wt% S and 101 ppm Se, Luguet et al., 2004; König et al., 2014) to a DMM with 185 ppm S and 49 ppb Se (Yierpan et al., 2019), which reproduces Fani Maoré source with 350 ppm S and 80 ppb Se modelled in Figure 6 (red square). In model 2, a hypothetic primary magma with similar Se content as Fani Maoré parental melts (95 ppb), but lower S (900 ppm) assimilates S-rich sediments or external sulfur trapped in the crust. Mixing lines between this primary magma and potential crustal contaminants, including evaporite gypsum (20.8 wt% S and S/Se=10^7, Malisa (2001)), crustal pyrite (54 wt% S and 4,280 ppb Se, Lorand and Alard, (2011)) and hydrothermal sulfides (33.4 wt% S, 9.2 ppm Se) (Luguet et al., 2004) are shown. Numbers along the lines indicate the proportion (wt%) of contaminant in the mixture. In model 3, Fani Maoré parental melts are directly produced by 4% melting of a mantle with moderate S (185 ppm) and Se (40 ppb) (green square) within the range proposed for the DMM by Yierpan et al. (2019) (green arrow referring to the melting model shown in Figure 6). (a&b) Composition of Fani Maoré magma sources inferred from the melting model (Figure 6) are plotted (red, green and blue squares with corresponding compositions given in Figure 6). The DMM composition plotted here corresponds to the low Se (49±11 ppb) and Te (3.5±1.3 ppb) concentrations estimated by

Article in press

Yierpan et al. (2019) for a depleted MORB mantle with 170-200 ppm S, the high Se-Te estimates corresponding to the BSE values of Wang and Becker (2013).

Figure 8. S/Se versus Sm/Yb variations in submarine oceanic basalts. The Sm/Yb ratio of basalts records the proportion of melt produced within the garnet stability field (>80 km) relative to melts produced at shallower depth. Data from this study are shown together with literature data for MORB, OIB, oceanic plateau, arc, and back-arc glasses and whole rocks. Data source: Yi et al. (2000), Jenner et al. (2010, 2015), Lissner et al. (2014), Reekie et al. (2019), Kurzawa et al. (2019), Yierpan et al. (2019, 2021), Wieser et al., (2020), and unpublished MORB, Samoa, and Iceland data compiled by Jenner and Jennings (2025). Error bars (± 1 SD) are shown for Fani Maoré data (Table 1) where larger than symbol size.

Article in press

References

Alard, O., Griffin, W.L., Lorand, J.P., Jackson, S. and O'Reilly, S.R. (2000). Non-chondritic distribution of highly siderophile elements in mantle sulfide. *Nature* 407, 891–894. doi: 10.1038/35038049

Berthod, C., Médard, E., Bachèlery, P., Gurioli, L., Di Muro, A., Peltier, A., Komorowski, J.-C., Benbakkar, M., Devidal, J.-L., Langlade, J., Besson, P., Boudon, G., Rose-Koga, E., Deplus, C., Le Friant, A., Bickert, M., Nowak, S., Thinon, I., Burckel, P., Hidalgo, S., Kaliwoda, M., Jorry, S.J., Fouquet, Y. and Feuillet, N. (2021). The 2018-ongoing Mayotte submarine eruption: magma migration imaged by petrological monitoring. *Earth and Planetary Science Letters* 571, 117085. doi: 10.1016/j.epsl.2021.117085

Berthod, C., Komorowski, J.-C., Gurioli, L., Médard, E., Bachèlery, P., Besson, P., Verdurme, P., Chevrel, O., Di Muro, A., Peltier, A., Devidal, J.-L., Nowak, S., Thinon, I., Burckel, P., Hidalgo, S., Deplus, C., Loubrieu, B., Pierre, D., Bermell, S., Pitel-Roudaut, M., Réaud, Y., Fouchard, S., Bickert, M., Le Friant, A., Paquet, F., Feuillet, N., Jorry, S.L., Fouquet, Y., Rinnert, E., Cathalot, C. and Lebas, E. (2022). Temporal magmatic evolution of the Fani Maoré submarine eruption 50 km east of Mayotte revealed by in situ sampling and petrological monitoring. *Comptes Rendus Géoscience* 354, 195–223. doi: 10.5802/crgeos.155

Brearley, M. and Scarfe, C.M. (1986) Dissolution Rates of Upper Mantle Minerals in an Alkali Basalt Melt at High Pressure: An Experimental Study and Implications for Ultramafic Xenolith Survival. *Journal of Petrology* 27, 1157–1182. doi:10.1093/petrology/27.5.1157

Brenan, J. M. (2015). Se–Te fractionation by sulfide–silicate melt partitioning: implications for the composition of mantle derived magmas and their melting residues. *Earth and Planetary Science Letters* 422, 45–57. doi: 10.1016/j.epsl.2015.04.011

Cathalot, C., Rinnert, E., Scalabrin, C., Fandino, O., Giunta, T., Ondreas, H., Rouxel, O., Rabouille, C., Dumoulin, J.-P., Bombled, B., Manoux, M., Walker, S., Chavagnac, V., Rizzo, A., Tardivel, M., Prado, E., Rawke, M.E., Mastin, M., Donval, J.-P., Guyader, V., Page, G., Matabos, M. and Feuillet, N. (2026). Large CO_2 seeps and hydrate field on the seafloor offshore Mayotte Island. *Nature Geoscience* 19, 759–762. doi: 10.1038/s41561-026-02004-2

Chauvel, C., Inglis, E. C., Gutierrez, P., Luu, T.-H., Burckel, P. and Besson, P. (2024). Fani Maoré, a new "young HIMU" volcano with extreme geochemistry, *Earth and Planetary Science Letters* 626, 118529. doi: 10.1016/j.epsl.2023.118529

Article in press

Chowdhury, P., Dasgupta, R., Phelps P. R., Lee, C.-T. A. and Anselm, R.A. (2021) Partitioning of chalcophile and highly siderophile elements (HSEs) between sulfide and carbonated melts – Implications for HSE systematics of kimberlites, carbonatites, and melt metasomatized mantle domains. *Geochimica et Cosmochimica Acta* 305, 130–147. doi: 10.1016/j.gca.2021.05.006

Class, C. and Goldstein, S.L. (1997). Plume-lithosphere interactions in the ocean basins: constraints from the source mineralogy. *Earth and Planetary Science Letters* 150, 245–260. doi: 10.1016/S0012-821X(97)00089-7

Class, C., Goldstein, S.L., Altherr, R. and Bachelery, P. (1998). The process of Plume–Lithosphere interactions in the Ocean Basins — The case of Grande Comore. *Journal. of Petrology* 39, 881–903. doi: 10.1093/petroj/39.5.881

Class, C., Goldstein, S., Stute, M., Kurz, M. and Schlosser, P. (2005). Grand Comore Island: A well-constrained "low $^{3}He/^{4}He$" mantle plume. *Earth and Planetary Science Letters* 233, 391–409. doi: 10.1016/j.epsl.2005.02.029

Dofal, A., Michon, L., Fontaine, F.R., Rindraharisaona, E., Barruol G. and Tkalčić, H. (2023). Imaging the lithospheric structure and plumbing system below the Mayotte volcanic zone. *Comptes Rendus Géoscience* 2023, 354, 47 - 64. doi: 10.5802/crgeos.190.

Edmonds M. and Mather T.A. (2017). Volcanic Sulfides and Outgassing. *Elements* 13, 105–110. doi: 10.2113/gselements.13.2.105

Emerick, C.M. and Duncan, R.A. (1982). Age progressive volcanism in the Comores Archipelago, western Indian Ocean and implications for Somali plate tectonics. *Earth and Planetary Science Letters* 60, 415–428. doi: 10.1016/0012-821X(82)90077-2

Famin, V., Michon, L. and Bourhane, A. (2020). The Comoros archipelago: a right-lateral transform boundary between the Somalia and Lwandle plates. *Tectonophysics* 789, 228539. doi: 10.1016/j.tecto.2020.228539

Feuillet, N., Jorry, S., Crawford, W.C., Deplus, C., Thinon, I., Jacques, E., Saurel, J.M., Lemoine, A., Paquet, F., Satriano, C., Aiken, C., Foix, O., Kowalski, P., Laurent, A., Rinnert, E., Cathalot, C., Donval, J.-P., Guyader, V., Gaillot, A., Scalabrin, C., Moreira, M., Peltier, A., Beauducel, F., Grandin, R., Ballu, V., Daniel, R., Pelleau, P., Gomez, J., Besançon, S., Geli, L., Bernard, P., Bachèlery, P., Fouquet, Y., Bertil, D., Lemarchand, A., and Van der Woerd, J. (2021). Birth of a large volcanic edifice offshore Mayotte via lithosphere-scale dyke intrusion. *Nature Geoscience* 14, 787–795. doi: 10.1038/s41561-021-00809-x

Forrest, A., Kelley K.A. and Schilling, J.G. (2017). Selenium, tellurium and sulfur variations in basalts along the Reykjanes Ridge and extension over Iceland, from 50°N to 65°N. *Interdisciplinary Earth Data Alliance (IEDA)*. doi: 10.1594/IEDA/100700.

Article in press

Fux, M., Schmidt, M. W., and Liebske, C. (2025) Redox melting of garnet lherzolite: Generation of carbonated silicate and sulfide melts and implications for OIB formation from chalcophile and redox-sensitive elements. Geochemistry, Geophysics, Geosystems 26, e2024GC012025. doi: 10.1029/2024GC012025

Greaney, l.T., Rudnick, R.L., Helz, R.T., Gaschnig, R.M., Piccoli, P.M. and Ash, R.D. (2017). The behavior of chalcophile elements during magmatic differentiation as observed in Kilauea Iki lava lake, Hawaii. *Geochimica et Cosmochimica Acta* 210, 71-96. doi: 10.1016/j.gca.2017.04.033

Greenland, L.P. and Aruscavage, P. (1986). Volcanic emission of Se, Te, and As from Kilauea volcano, Hawaii. *Journal Volcanology and Geothermal Research* 27, 195-201. doi: 10.1016/0377-0273(86)90086-7

Hajash, A. and Armstrong, R.L. (1972). Paleomagnetic and radiometric evidence for the age of the Comores Islands, west central Indian Ocean. *Earth and Planetary Science Letters* 16, 231–236. doi: 10.1016/0012-821X(72)90195-1

Helmy, H.M., Ballhaus, C., Wohlgemuth-Ueberwasser, C., Fonseca, R.O.C. and Laurenz, V. (2010). Partitioning of Se, As, Sb, Te and Bi between monosulfide solid solution and sulfide melt – Application to magmatic sulfide deposits. *Geochimica Cosmochimica Acta* 74, 6174-6179. doi: 10.1016/j.gca.2010.08.009

Jenner, F.E., O'Neill, H.S.C., Arculus, R.J. and Mavrogenes, J.A. (2010). The magnetite crisis in the evolution of Arc-related magmas and the initial concentration of Au, Ag and Cu. *Journal. of Petrology* 51, 2445–2464. doi: 10.1093/petrology/egq063

Jenner, F.E., Hauri, E.H., Bullock, E.S., König, S., Arculus, R. J., Mavrogenes, J. A., Mikkelson, N. and Goddard, C. (2015). The competing effects of sulfide saturation versus degassing on the behavior of the chalcophile elements during the differentiation of hydrous melts. *Geochemistry Geophysics Geosystems* 16, 1490–1507, doi: 10.1002/2014GC005670.

Jenner, F.E. and Jennings, E.S. (2025). The use of geochemistry for placing constraints on mantle melting processes and the evolution of mantle heterogeneity, in: Anbar, A., Weis, D. (Eds.), *Treatise on Geochemistry (Third edition)*. Elsevier, Oxford, pp. 333-380. doi: 10.1016/B978-0-323-99762-1.00091-7

Jochum, K.P., Nohl, U., Herwig, K., Lammel, E., Stoll, B. and Hofmann A.W. (2005). GeoReM: A New Geochemical Database for Reference Materials and Isotopic Standards. *Geostandards and Geoanalytical Research* 29, 333-338. doi: 10.1111/j.1751-908X.2005.tb00904.x

Kiseeva E.S., Fonseca R.O.C. and Smythe D. J. (2017). Chalcophile elements and sulfides in the upper mantle. *Elements* 13, 111–116. doi: 10.2113/gselements.13.2.111

Article in press

König, S, Lorand, J.-P., Luguet, A. and Pearson, D.G. (2014). A non-primitive origin of near-chondritic S–Se–Te ratios in mantle peridotites; implications for the Earth's late accretionary history. *Earth and Planetary Science Letters* 385, 110-121. doi: 10.1016/j.epsl.2013.10.036

König, S, Lissner, M., Lorand, J.-P., Bragagni, A., Luguet, A. (2015). Mineralogical control of selenium, tellurium and highly siderophile elements in the Earth's mantle: Evidence from mineral separates of ultra-depleted mantle residues. *Chemical Geology* 396, 16–24. doi: 10.1016/j.chemgeo.2014.12.015

Kurzawa, T., König, S., Alt, J.C., Yierpan, A. and Schoenberg, R. (2019). The role of subduction recycling on the selenium isotope signature of the mantle: Constraints from Mariana arc lavas. *Chemical Geology* 513, 239–249. doi: 10.1016/j.chemgeo.2019.03.011

Lissner, M., König, S., Luguet, A., le Roux, P.-J., Schuth, S., Heuser, A. and le Roex, A.-P. (2014). Selenium and tellurium systematics in MORBs from the southern Mid-Atlantic Ridge (47–50°S). *Geochimica Cosmochimica et Acta* 144, 379–402. doi: 10.1016/j.gca.2014.08.023

Liu, Z. and Li, Y. (2025). The partitioning of selenium and tellurium between sulfide liquid and silicate melt and their abundances in the silicate Earth. *Earth and Planetary Science Letters* 656, 119277. doi: 10.1016/j.epsl.2025.119277

Lorand, J.-P. and Alard, O. (2010). Determination of selenium and tellurium concentrations in Pyrenean peridotites (Ariege, France): new insight into S/Se/Te systematics of the upper in mantle samples. *Chemical Geology* 278, 120–130. doi: 10.1016/j.chemgeo.2010.09.007

Lorand, J.-P. and Alard, O. (2011). Pyrite tracks assimilation of crustal sulfur in Pyrenean peridotites. *Mineralogy and Petrology* 101, 115–128. doi: 10.1007/s00710-010-0138-2

Luguet, A., Lorand, J.P., Alard, O. and Cottin, J.Y. (2004). A multi-technique study of platinum group element systematic in some Ligurian ophiolitic peridotites, Italy. *Chemical Geology* 208, 175–194. doi: 10.1016/j.chemgeo.2004.04.011

Maier, W.D. and Barnes, S.-J. (2010). The Kabanga Ni sulfide deposits, Tanzania: II. Chalcophile and sidérophile element geochemistry. *Mineral. Deposita* 45, 443–460. doi: 10.1007/s00126-010-0283-x

Malisa, E.P. (2001). The Behaviour of Selenium in Geological Processes. *Environmental Geochemistry and Health* 23, 137–158. doi: 10.1023/A:1010908615486

Mason, E., Wieser, P.E., Liu, E.J., Edmonds, M., Ilyinskaya, E., Whitty, R.C.W., Mather, T.A., Elias, T., Nadeau, P.A., Wilkes, T.C., McGonigle, A.J.S., Pering, T.D., Mims, F.M., Kern C., Schneider, D.J. and Oppenheimer, C. (2021). Volatile metal emissions from volcanic degassing and lava–seawater interactions at Kīlauea Volcano, Hawai'i. *Communications Earth Environment* 2, 79. doi: 10.1038/s43247-021-00145-3

Article in press

Merle, R., Caroff, M., Girardeau, J., Cotton, J. and Guivel, C. (2005). Segregation vesicles, cylinders, and sheets in vapor-differentiated pillow lavas: examples from Tore-Madeira Rise and Chile Triple Junction, *Journal Volcanology and Geothermal Research* 141, 109-122. doi: 10.1016/j.jvolgeores.2004.09.007

Michon, L. (2016). The volcanism of the Comores archipelago integrated at a regional scale. In: Bachèlery, P., Lénat, J.-F., Di Muro, A., Michon, L. (Eds.), *Active Volcanoes of the Southwest Indian Ocean: Piton de La Fournaise and Karthala*. Springer-Verlag, Berlin and Heidelberg, pp. 333–344. doi: 10.1007/978-3-642-31395-0_21

Nougier, J., Cantagrel, J.M. and Karche, J.P. (1986). The Comores archipelago in the western Indian Ocean: volcanology, geochronology and geodynamic setting. *Journal of African Earth Sciences* 5, 135–145. doi: 10.1016/0899-5362(86)90003-5

Patten, C., Barnes, S. J., Mathez, E. A. and Jenner, F.E. (2013). Partition coefficients of chalcophile elements between sulfide and silicate melts and the early crystallization history of sulfide liquid: LA-ICP-MS analysis of MORB sulfide droplets. *Chemical Geology* 358, 170–188. doi: 10.1016/j.chemgeo.2013.08.040.

Pelleter, A.-A., Caroff, M., Cordier, C., Bachèlery, P., Nehlig, P., Debeuf, D. and Arnaud, N. (2014). Melilite-bearing lavas in Mayotte (France): An insight into the mantle source below the Comores. *Lithos* 208–209, 281–297. doi: 10.1016/j.lithos.2014.09.012

Philpotts, A.R. and Lewis, C.L. (1987). Pipe vesicles—An alternate model for their origin. *Geology* 15, 971–974. doi: 10.1130/0091-7613(1987)15<971:PVAMFT>2.0.CO;2

Queffurus, M. and Barnes, S.-J. (2015). A review of sulfur to selenium ratios in magmatic nickel–copper and platinum-group element deposits. *Ore Geology Reviews* 69, 301-324. doi: 10.1016/j.oregeorev.2015.02.019

Reekie, C.D.J., Jenner, F.E., Smythe, D.J., Hauri, E.H., Bullock, E.S. and Williams, H.M. (2019). Sulfide resorption during crustal ascent and degassing of oceanic plateau basalts. *Nature Communications* 10, 82. doi: 10.1038/s41467-018-08001-3

Rehkämper, M., Halliday, A.N., Fitton, J.G., Lee, D.-C., Wieneke, M., Arndt, N.T. (1999). Ir, Ru, Pt, and Pd in basalts and komatiites: new constraints for the geochemical behavior of the platinum-group elements in the mantle. *Geochimica et Cosmochimica Acta* 63, 3915-3934. doi: 10.1016/S0016-7037(99)00219-7

Rinnert, E., Lebas, E., Paquet, F., Jorry, S., Feuillet, N., Thinon, I. and Fouquet, Y. (2019). MAYOBS cruises. doi: 10.18142/291.

Rinnert, E., Cathalot, C. and Feuillet, N. (2021). GEOFLAMME cruise, RV Pourquoi pas ? doi: 10.17600/18001297.

Article in press

Rubin, K., (1997). Degassing of metals and metalloids from erupting seamount and mid-ocean ridge volcanoes: Observations and predictions. *Geochimica et Cosmochimica Acta* 61, 3525–3542. doi: 10.1016/S0016-7037(97)00179-8

Ryan, W.B.F., Carbotte, S.M., Coplan, J.O., O'Hara, S., Melkonian, A., Arko, R., Weissel, R.A., Ferrini, V., Goodwillie, A., Nitsche, F., Bonczkowski, J., and Zemsky, R. (2009). Global Multi-Resolution Topography synthesis, *Geochemistry Geophysics Geosystems* 10, Q03014, doi: 10.1029/2008GC002332

Shannon R.D. (1976). Revised effective ionic radii and systematic studies of interatomic distances in halides and chalcogenides. *Acta Crystallographica* A32, 751–767. doi: 10.1107/S0567739476001551

Thinon, I., Lemoine, A., Leroy, S., Paquet, F., Berthod, C., Zaragosi, S., Famin, V., Feuillet, N., Boymond, P., Masquelet, C., Mercury, N., Rusquet, A., Scalabrin, C., Van der Woerd, J., Bernard, J., Bignon, J., Clouard, V., Doubre, C., Jacques, E., Jorry, S.J., Rolandone, F., Chamot-Rooke, N., Delescluse, M., Franke, D., Watremez, L., Bachèlery, P., Michon, L., Sauter, D., Bujan, S., Canva, A., Dassie, E., Roche, V., Ali, S., Sitti Allaouia, A.H., Deplus, C., Rad, S. and Sadeski, L. (2022). Volcanism and tectonics unveiled in the Comoros Archipelago between Africa and Madagascar. *Comptes Rendus Géoscience* 354, 1–28. doi: 10.5802/crgeos.159

Verdurme, P., Gurioli, L., Chevrel, O., Médard, E., Berthod, C., Komorowski, J.-C., Harris, A., Paquet, F., Cathalot, C., Feuillet, N., Lebas, E., Rinnert, E., Donval, J.-P., Thinon, I., Deplus, C. and Bachèlery, P. (2024). Magma ascent and lava flow field emplacement during the 2018–2021 Fani Maoré deep-submarine eruption insights from lava vesicle textures. *Earth and Planetary Science Letters* 636, 118720. doi: 10.1016/j.epsl.2024.118720

Vlastélic. I., Menard, G., Gannoun, M., Piro, J.-L., Staudacher, T. and Famin, V. (2013). Magma degassing during the April 2007 collapse of Piton de la Fournaise: the record of semi-volatile trace elements (Li, B, Cu, In, Sn, Cd, Re, Tl, Bi). *Journal of Volcanology and Geothermal Research* 254, 94-107. doi: 10.1016/j.jvolgeores.2012.12.027

Vlastélic, I. and Piro, J.-L. (2022). Volatilization of trace elements during evaporation to dryness of HF-dissolved silicates (BHVO-2, AGV-1, BIR-1, UB-N): Open versus closed system conditions. *Geostandards and Geoanalytical Research* 46, 519-534. doi: 10.1111/ggr.12428

Wang, Z. and Becker, H. (2013). Ratios of S, Se and Te in the silicate Earth require a volatile-rich late veneer. *Nature* 499, 328–331. doi: 10.1038/nature12285

Article in press

Wawrzyniak, P., Gaillard, F., Hautot, S., Andujar, J., Tarits, P., Arbaret, L., Guegan, S., Sifré, D., D'Eu, J.-F., Deparis, J., Lemoine, A., Thinon, I., Warden, S. and Dubois, F. (2025). Magnetotelluric evidence for a melt-rich magmatic reservoir beneath Mayotte. *Nature* 646, 1122–1128. doi: 10.1038/s41586-025-09625-4

Wieser, P.E., Jenner, F., Edmonds, M., Maclennan, J., Kunz, B.E. (2020). Chalcophile elements track the fate of sulfur at Kīlauea Volcano, Hawai'i. *Geochimica et Cosmochimica Acta* 282, 245-275. doi: 10.1016/j.gca.2020.05.018

Xue, S. and Li, Y. (2025) The partitioning of chalcophile and siderophile elements (CSEs) between sulfide liquid and carbonated melt. *Geochimica et Cosmochimica Acta* 388, 94–113. doi: 10.1016/j.gca.2024.11.019

Yi, W., Halliday, A. N., Alt, J.C., Lee, D.-C., Rehkämper, M., Garcia, M.O., Langmuir, C.H. and Su, Y. (2000). Cadmium, indium, tin, tellurium, and sulfur in oceanic basalts: implications for chalcophile element fractionation in the Earth. *Journal of Geophysical Research* 105, 18927-18948. doi: 10.1029/2000JB900152

Yierpan, A., König, S., Labidi, J., Kurzawa, T., Babechuk, M. G. and Schoenberg, R. (2018). Chemical sample processing for combined selenium isotope and selenium- tellurium elemental investigation of the Earth's igneous reservoirs. *Geochemistry Geophysics Geosystems* 19, 516–533. doi: 10.1002/2017GC007299

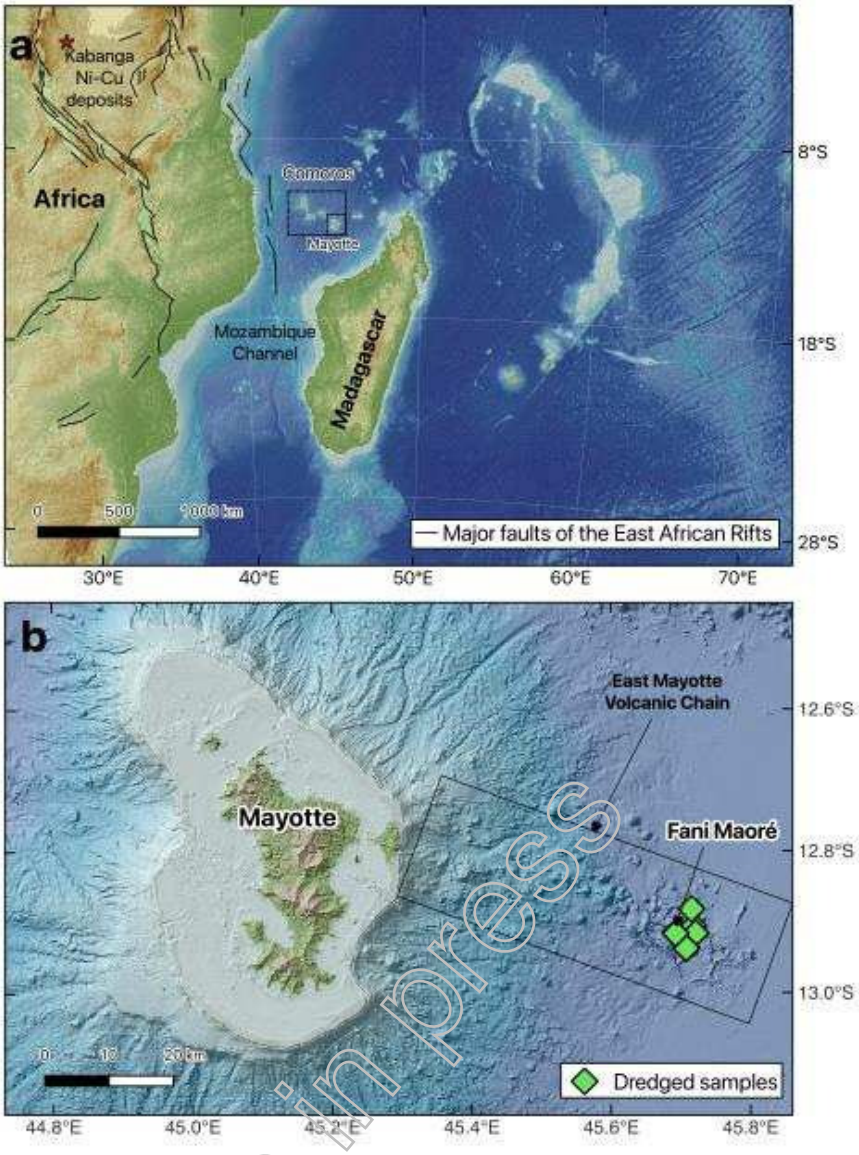
Yierpan, A., König, S., Labidi, J. and Schoenberg, R. (2019). Selenium isotope and S-Se-Te elemental systematics along the Pacific-Antarctic ridge: Role of mantle processes. *Geochimica et Cosmochimica Acta* 249, 199–224. doi: 10.1016/j.gca.2019.01.028

Yierpan, A., Redlinger, J. and König, S. (2021). Selenium and tellurium in Reykjanes Ridge and Icelandic basalts: evidence for degassing-induced Se isotope fractionation. *Geochimica et Cosmochimica Acta* 313, 155–172. doi: 10.1016/j.gca.2021.07.029

Zelenski, M., Simakin, A., Taran, Y., Kamenetsky, V.S. and Malik, N. (2021). Partitioning of elements between high-temperature, low-density aqueous fluid and silicate melt as derived from volcanic gas geochemistry. *Geochimica et Cosmochimica Acta* 295, 112–134. doi: 10.1016/j.gca.2020.12.011

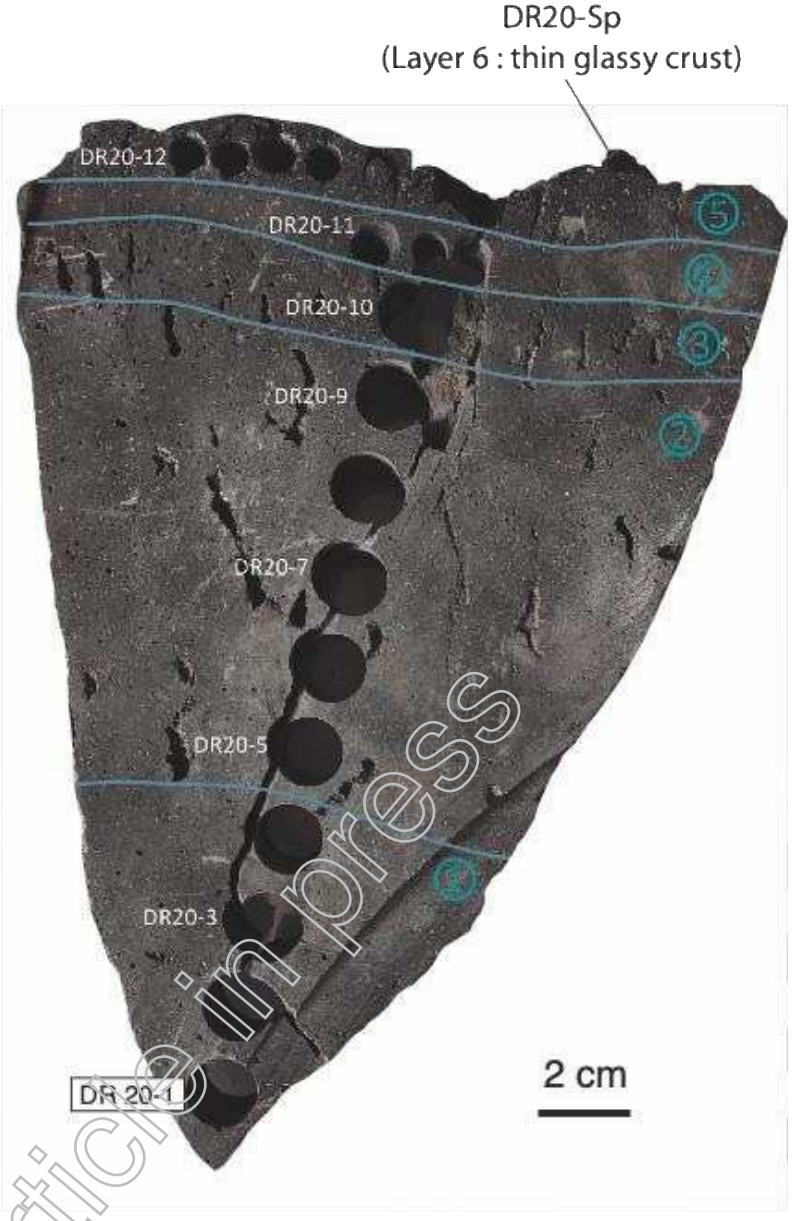
Zhang Z. and Hirschmann M. M. (2016) Experimental constraints on mantle sulfide melting up to 8 GPa. *American Mineralogist* 101, 181–192. doi: 10.2138/am-2016-5308

Article in press



Article in press

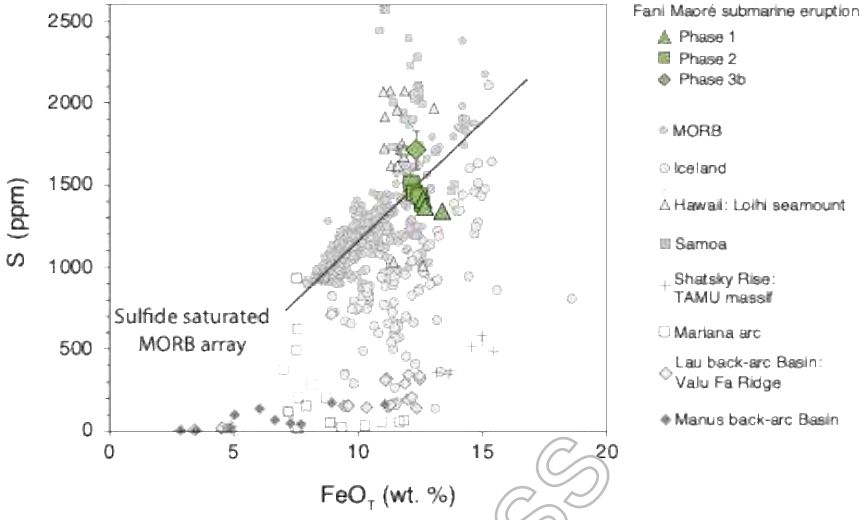
F2



Article in press

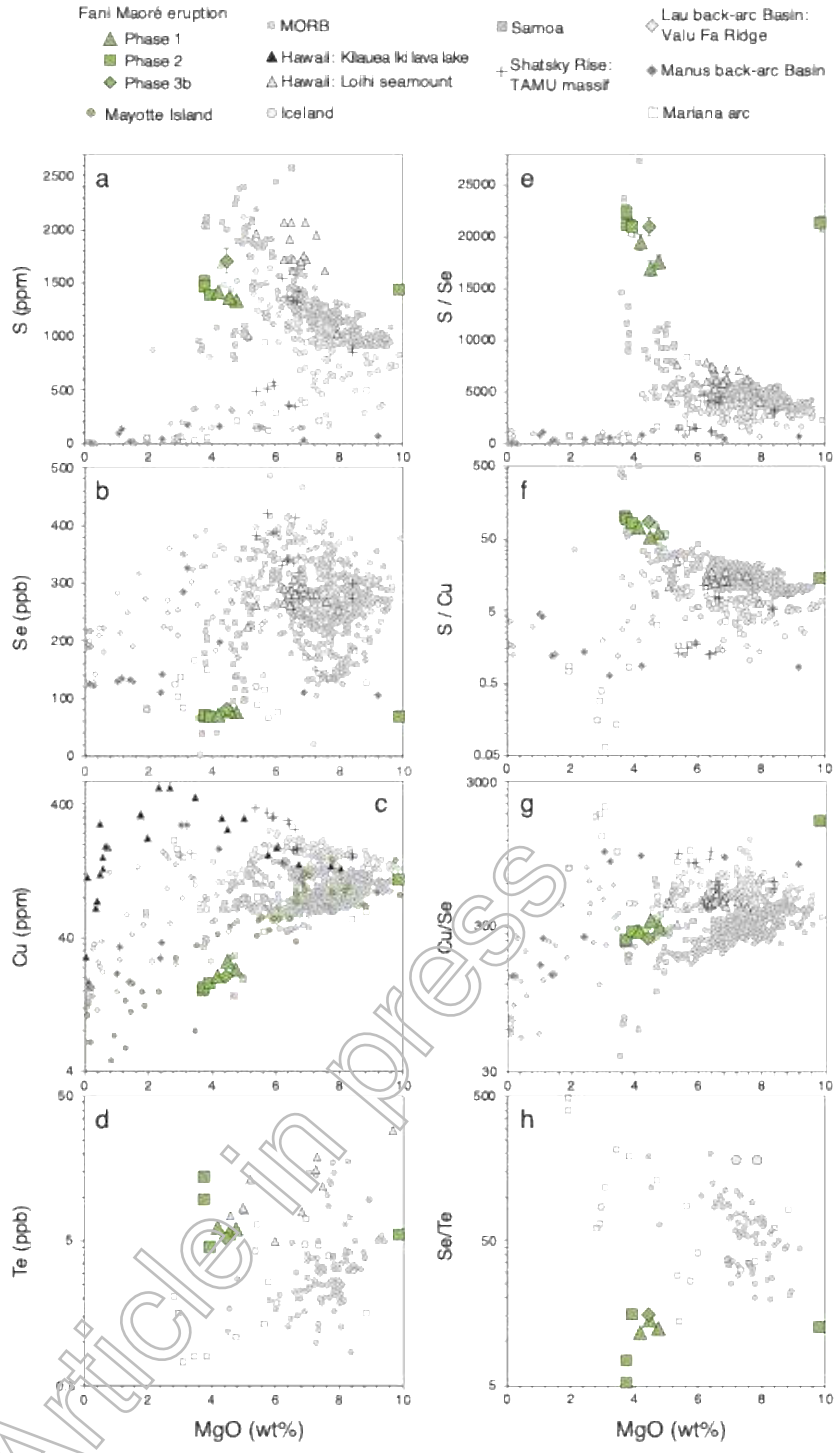
780

F3

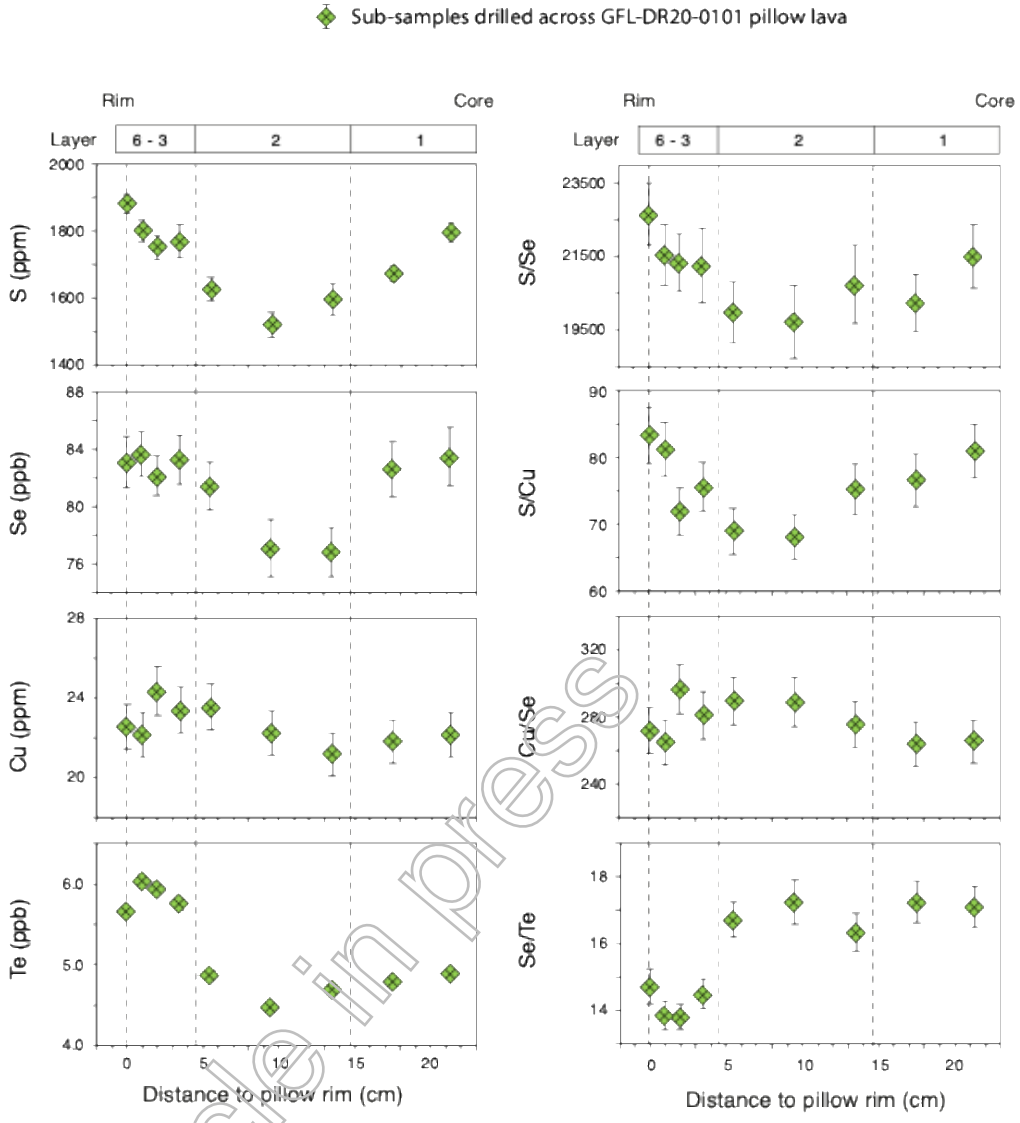


Article in press

F4



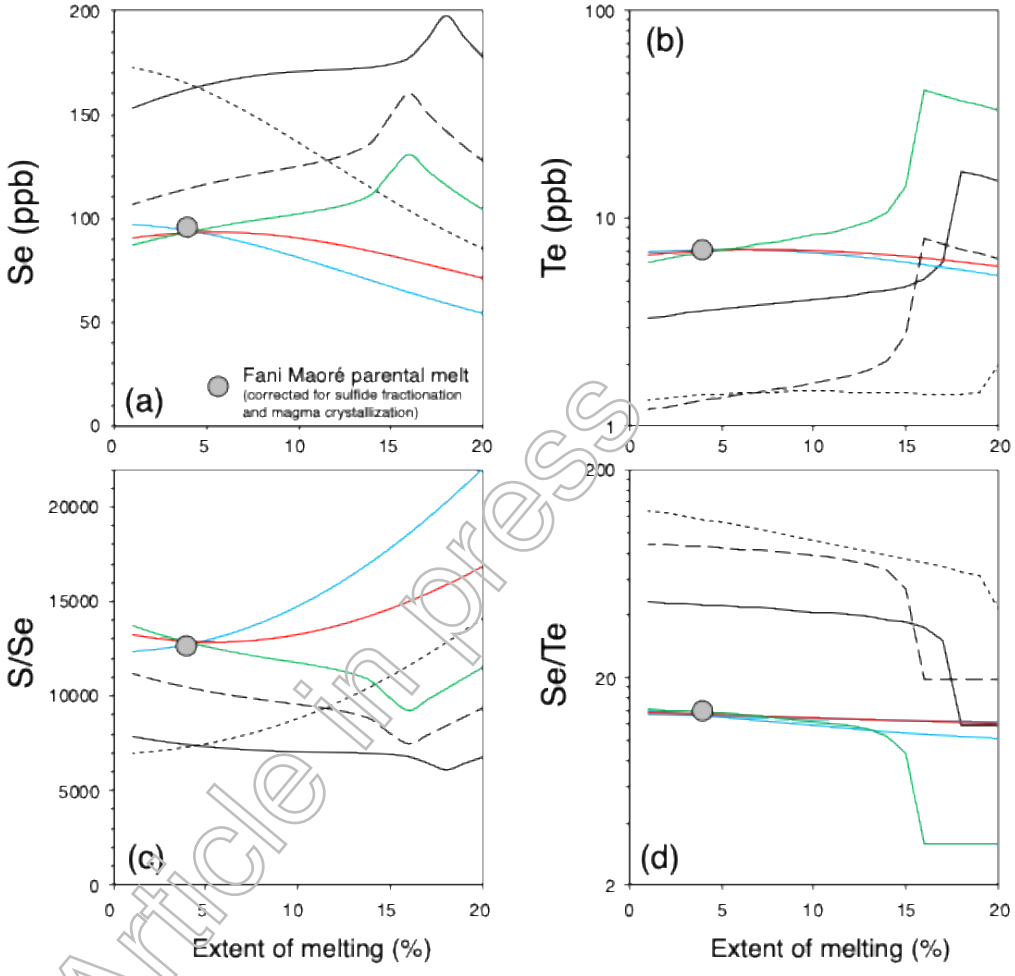
Article in press



Article in press

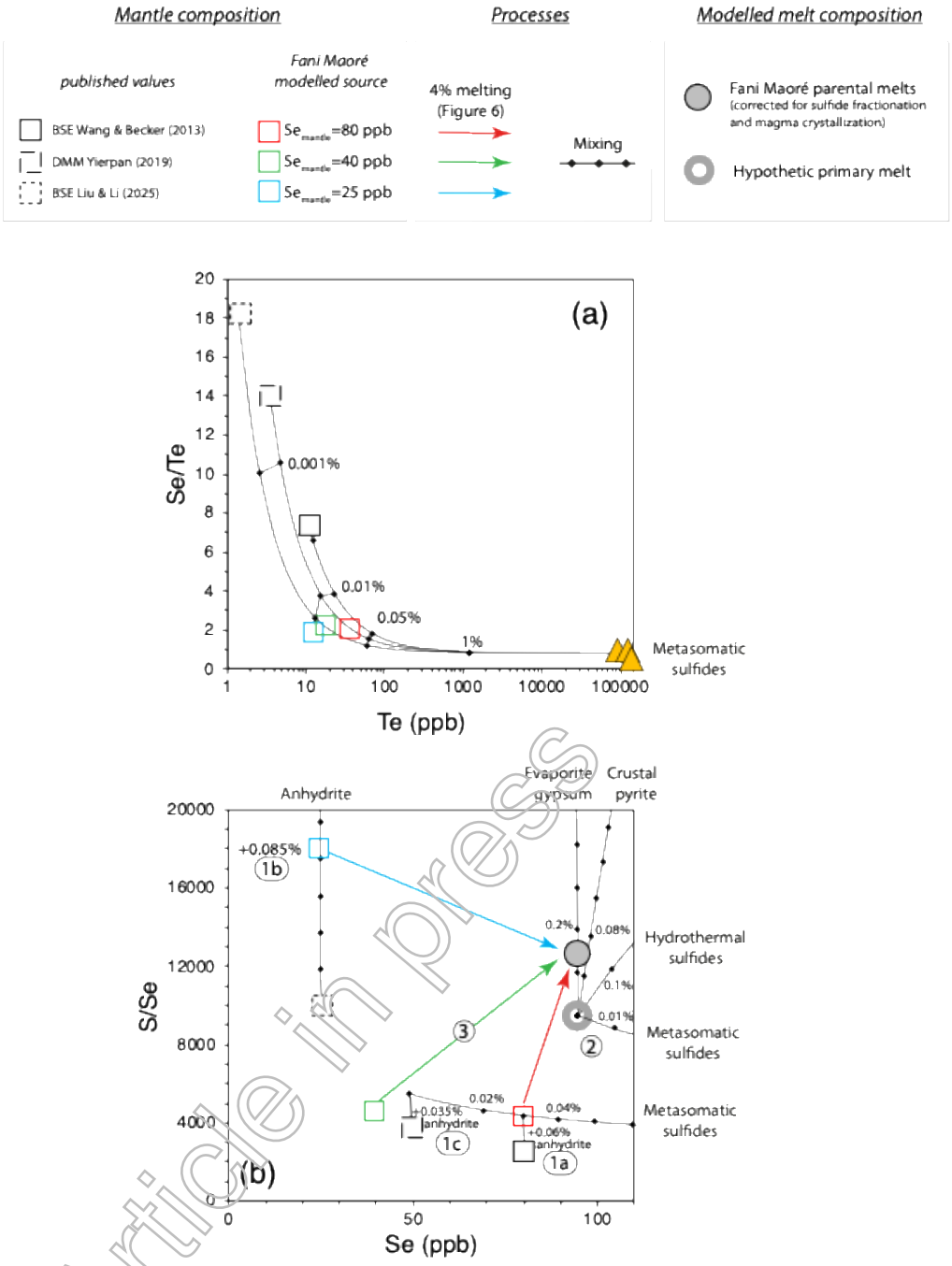
F6

	Mantle composition						Melt composition				
	S_{mantle} (ppm)	Se_{mantle} (ppb)	Te_{mantle} (ppb)	S/Se_{mantle}	Se/Te_{mantle}		K_{Se} SL/SM	K_{Se} SL/CSM	K_{Te} SL/SM	K_{Te} SL/CSM	
Published values											
BSE Wang & Becker (2013)	211	80	11	2,638	7.3			914		5906	
DMM Yierpan (2019)	185	49	3.5	3,776	14			914		5906	
BSE Liu &Li (2025)	250	25	1.37	10,000	18.2		200		1500		
Composition fitting Fani Maoré parental melt at $F_{melting}$=4%											
Se_{mantle}=80 ppb	350	80	38	4,375	2.11			914		5906	
Se_{mantle}=40 ppb	185	40	18	4,625	2.22			914		5906	
Se_{mantle}=25 ppb	450	25	13	18,000	1.92		200		1500		



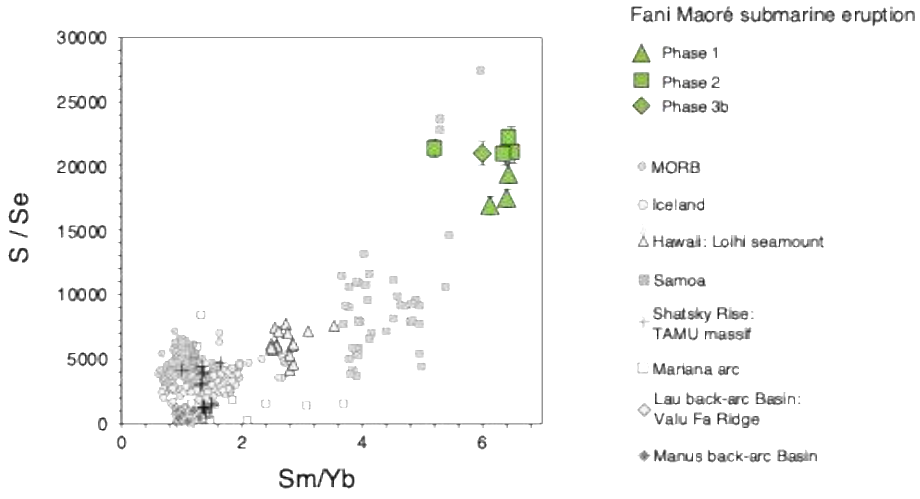
Article in press

F7



Article in press

F8



Article in press

Table 1: S, Se and Te concentrations of reference materials and rock samples from Fani Maoré volcano, Mayotte.

Sample	Lat. (°S)	Long. (°E)	Depth (m)	Eruption phase**	MgO (wt%)	$Fe_2O_3^{(T)}$ (wt%)	Cu (ppm)	S (ppm)	1SD		Se (ppb)	1SD		Te (ppb)	1SD	
BHVO-2					7.26			185	± 7	(n=10)	170	± 11	(n=20)	14.52	± 0.77	(n=14)
BCR-2					3.60			341	± 1	(n=2)	79.6	± 0.8	(r=3)	2.84	± 0.07	(r=3)
BE-N					13.15			336	± 5	(r=1)	71.7	± 0.9	(r=1)	1.06	± 0.01	(r=2)
BIR-1					9.70			4.43	± 0.04	(r=3)	16.1	± 0.04	(r=2)	5.90	± 0.06	(r=1)
MAY01-DR01-05	-12.9067	45.7183	-2935	1	4.77	14.85	23.1	1342	± 32		76.7	± 1.1		6.15	± 0.06	
MAY04-DR12-0301	-12.8822	45.7155	-3222	1	4.52	14.10	27.1	1367	± 39		80.7	± 1.3		5.71	± 0.06	
MAY04-DR10-07	-12.9165	45.7212	-3035	1	4.18	14.02	20.5	1413	± 41		72.8	± 1.0		6.26	± 0.05	
MAY04-DR11-0704-2	-12.9167	45.6927	-3239	2	3.97	13.94	18.1	1386	± 32		66.5	± 1.2		4.43	± 0.06	
MAY04-DR11-0704	-12.9167	45.6927	-3239	2	9.89	13.84	106	1430	± 25		67.3	± 1.1		5.48	± 0.06	
MAY02-DR08-0102MB	-12.9375	45.7080	-3061	2	3.79	13.65	16.7	1454	± 32		69.4	± 1.0		13.6	± 0.10	
MAY02-DR08-01ALF	-12.9375	45.7080	-3061	2	3.77	13.49	15.9	1509	± 40		68.2	± 1.1		9.53	± 0.07	
GFL-DR20-0101 Bulk	-12.8693	45.6715	-3179	3b	4.45	13.70	20.6	1711*	± 117*		81.5*	± 2.7*		5.23*	± 0.60*	
GFL-DR20-0101 Drilling	Distance to pillow rim (cm)															
DR20-1	21.3 cm						22.1	1794	± 30	(n=2)	83.5	± 2.1	(n=2)	4.89	± 0.05	(n=2)
DR20-3	17.5 cm						21.8	1671	± 26		82.6	± 2.0		4.79	± 0.06	
DR20-5	13.5 cm						21.2	1593	± 47		76.8	± 1.7		4.70	± 0.06	
DR20-7	9.5 cm						22.3	1518	± 37		77.0	± 2.0		4.47	± 0.05	
DR20-9	5.5 cm						23.5	1625	± 34		81.4	± 1.6		4.87	± 0.05	
DR20-10	3.5 cm						23.4	1768	± 49	(n=2)	83.2	± 1.7	(n=2)	5.75	± 0.06	(n=2)
DR20-11	2 cm						24.3	1751	± 35		82.1	± 1.4		5.94	± 0.06	
DR20-12	1 cm						22.1	1801	± 35		83.6	± 1.6		6.04	± 0.08	
DR20-SP	0 cm						22.6	1881	± 30	(n=2)	83.1	± 1.8	(n=2)	5.65	± 0.07	(n=2)

** Eruption phase : Phase 1 (July 2018 - May 2019) ; Phase 2 (May 2019 - August 2019) ; Phase 3b (October 2020 - January 2021)

n: dissolution & chemistry duplicate

r : analysis replicate (same solution)

SD : standard deviation is calculated by propagating errors on isotopic ratios (see text) or calculated based on repeated analyses (n or r >1)

* Mean composition and 1SD of the 9 drilled samples from GFL-DR20-0101

MgO, $Fe_2O_3^{(T)}$ and Cu data are from Berthod et al. (2022) and Chauvel et al. (2024) (studied samples), USGS and CRPG (Reference Materials) and this work (GFL-DR20-0101 Drilling)

Article in press